2014

Experimental and Numerical Investigations of Microdroplet Evaporation with a Forced Pinned Contact Line

Kevin Gleason
University of Central Florida

EXPERIMENTAL AND NUMERICAL INVESTIGATIONS OF MICRODROPLET EVAPORATION WITH A FORCED PINNED CONTACT LINE.

by

KEVIN GLEASON

A thesis submitted in partial fulfillment of the requirements
for the Honors in the Major Program in Aerospace Engineering
in the College of Engineering and Computer Science
and in the Burnett Honors College
at the University of Central Florida
Orlando, Florida

Spring Term 2014

Thesis Chair: Shawn A. Putnam

ABSTRACT

Experimental and numerical investigations of water microdroplet evaporation on heated, laser patterned polymer substrates are reported. The study is focused on both (1) validating numerical models with experimental data, (2) identifying how changes in the contact line influences evaporative heat transfer and (3) determining methods of controlling contact line dynamics during evaporation. Droplets are formed using a bottom-up methodology, where a computer-controlled syringe pump supplies water to a $\sim$200μm in diameter fluid channel within the heated substrate. This methodology facilitates precise control of the droplets growth rate, size, and inlet temperature. In addition to this microchannel supply line, the substrate surfaces are laser patterned with a moat-like trench around the fluid-channel outlet, adding additional control of the droplets contact line motion, area, and contact angle. In comparison to evaporation on non-patterned substrate surfaces, this method increases the contact line pinning time by $\sim$60% of the droplets lifetime. The evaporation rates are compared to the predictions of a commonly reported model based on a solution of the Laplace equation, providing the local evaporation flux along the droplets liquid-vapor interface. The model consistently overpredicts the evaporation rate, which is presumable due to the models constant saturated vapor concentration along the droplets liquid-vapor interface. In result, a modified version of the model is implemented to account for variations in temperature along the liquid-vapor interface. A vapor concentration distribution is then imposed using this temperature distribution, increasing the accuracy of predicting the evaporation rate by $\sim 7.7\%$ and $\sim 9.9\%$ for heated polymer substrates at $T_s = 50$℃ and 65℃, respectively.

ACKNOWLEDGMENTS

I cannot express my appreciation for all the support, encouragement, and knowledge my adviser, Dr. Shawn Putnam, has provided me. His confidence in my abilities far exceeded my own and helped me realize my own potential, all while ensuring I maintained my sanity. I am thankful for the excellent mentorship he has provided over the past semesters, and look forward to furthering my academic success with him. I would also like to thank my thesis committee members Dr. Weiwei Deng and Dr. Lei Zhai, for their time and support.

Special thanks to Alan Nehemy, whos astonishing creativity was more than amusing, but immensely helpful within the lab. His knowledge and generosity provided an excellent learning environment, which I am grateful for.

I would also like to acknowledge and thank Adam Phillips, who shared the misery and unexpected stress levels of writing a thesis. I appreciate the help in the occasional battles against LaTeX, in addition to sharing the countless, long, and frigid all-nighters in the lab. While our constant ranting may have been counterproductive, I believe we both have completed successful theses and will do the same next year.

I wish Josh Murdock the best of luck in completing his HIM thesis, who has the potential to produce outstanding work. Additionally, I look forward to continuing my work with Harish Voota as we write our Masters theses.

Additional thanks to all my friends and classmates, all who unknowingly helped by forcing me to be socially active. I extend my thanks to the Burnett Honors College, Department of Mechanical and Aerospace Engineering, and the Office of Undergraduate Research for the opportunities, support, and guidance they provided me.

TABLE OF CONTENTS

LIST OF FIGURES

LIST OF TABLES

NOMENCLATURE

A	Area
A_f	Area Fraction
Bo	Bond Number
c	Vapor Concentration
c_s	Vapor Concentration at Liquid-Vapor Interface
c_∞	Ambient Vapor Concentration
D	Vapor Diffusion Coefficient
$\cancel{d}$	Diameter
$\cancel{d}_p$	Ablation Diameter
f_{eye}	Lens Focal Length
g	Gravity
H	Humidity
h	Height
i	Imaginary Number, $\sqrt{-1}$
J	Local Evaporation Flux
J_T	Total Evaporation Flux
$\mathfrak{M}$	Molar Mass
$\dot{m}_{lv}$	Evaporation Rate
l_c	Capillary Length
$\hat{n}$	Normal Vector
$\mathbb{P}$	Pressure
R	Contact Radius
R_c	Radius of Curvature

R_p	Substrate Pattern Radius
$\Re$	Universal Gas Constant
r	Radius Coordinate Definition
S	Surface Area
T	Temperature
T_{fit}	Surface Fitted Temperature
T_{iso}	Isotherm Temperature
T_s	Substrate Surface Temperature
$\not{V}$	Volume
Y	Surface Chemical Pattern
z	Height Coordinate Definition

Greek

α	Toroidal Coordinate
β	Toroidal Coordinate
γ	Surface Tension
γ_{lv}	Surface Tension at Liquid-Vapor Interface
γ_{sl}	Surface Tension at Solid-Liquid Interface
γ_{sv}	Surface Tension at Solid-Vapor Interface
δ_p	Ablation Depth
ϵ	Convergence Tolerance, 10^{-4}
η	Surface Roughness
θ	Contact Angle
θ_a	Advancing Contact Angle
θ_E	Effective Contact Angle

θ_r	Receding Contact Angle
Λ_{lv}	Latent Heat of Vaporization
λ	Wavelength
ξ	Integral Transform Variable
$\dot{\pi}_{lv}$	Evaporation Rate per Unit Contact Line Length
ρ	Density
τ	Integral Transform Variable
τ_D	Contact Line Depinning Time
τ_E	Droplet Lifetime
τ_P	Contact Line Pinning Time
ϕ	Azimuthal Angle Coordinate Definition

Acronyms

CAH	Contact Angle Hysteresis
CCA	Constant Contact Angle
CCD	Charge-Coupled Device
CCR	Constant Contact Radius
CHF	Critical Heat Flux
DAQ	Data Acquisition Board
EOM	Electro-Optic Modulator
PTFE	Polytetrafluoroethylene
μTAS	Micro-Total Analysis Systems

CHAPTER 1: INTRODUCTION

Droplet evaporation, a seemingly simple process, proves to be a rather complex multi-physical phenomenon with a wide range of technical applications including spray cooling [21], DNA/RNA microarray technology [22], inkjet printing [76], fuel injection and propulsion [62], and Micro-Total Analysis Systems (μTAS) [53]. DNA microarray production, for example, uses colloids drying along the droplets contact line for pattern production (commonly referred to as *coffee-ring effect*). However, the variability in droplet evaporation patterns poses concerns toward reliable implementation of this technology. Spray cooling, on the other hand, produces numerous microdroplets which impact a surface for cooling. This effective thermal management strategy must maintain high heat transfer rates, which are dictated by various droplet characteristics during impact and evaporation.

Recently, droplet evaporation studies have become attractive for evaluating the efficiency of heat removal. Small liquid drops are of special interest in relation to heat transfer due to their ability to remove large heat fluxes. During droplet evaporation, a majority of the heat transferred occurs within the vicinity of the solid-liquid interface (as opposed to the liquid-vapor interface). This is because the thermal resistance of the liquid-vapor interface is 10 to 50 times greater than at the solid-liquid interface [15, 58]. Wetted droplets have a large solid-liquid interface while maintaining a low thermal resistance, providing a high heat transfer coefficient. Non-wetted droplets (larger liquid-vapor interface) have a larger thermal resistance, giving a lower overall heat transfer coefficient and a corresponding smaller heat flux. Thus, a comprehensive understanding of both the dynamics of droplet formation and droplet evaporation are crucial for state-of-the-art advancements in new technologies.

1.1 Background

1.1.1 Droplet Statics and Dynamics

A liquid droplet resting on a solid horizontal surface, termed a sessile droplet, is characterized by its interaction with a solid and surrounding medium. Assuming the drop maintains a spherical shape (valid in the absence of gravity), the contact area between the drop and solid surface remains circular. Gravity effects can be neglected for droplets with a low Bond number ($\lesssim 0.1$) [56, 67, 68], or measuring the characteristic length smaller than the fluids capillary length. The bond number, $Bo = \Delta\rho g R h_0/\gamma_{lv}$, represents the importance of gravitational forces to surface tension forces; where $\Delta\rho$ is the difference in density between the liquid and surrounding vapor, R is the contact radius, h_0 is the initial drop height measured from the surface, and γ_{lv} represents the liquid-vapor surface tension. A low bond number ($Bo \lesssim 0.1$) indicates the surface tension forces are at least an order of magnitude larger than the gravitational forces. Similar conclusions are found when the capillary length, $l_c = \sqrt{\gamma_{lv}/\rho g}$, is $\lesssim 2.7$ mm for water at room temperature (20℃). With this, a spherical droplet approximation is accurate for micron-sized water droplets.

In addition to the contact area, the liquid drop is more commonly identified by one of two main states (wetting or non-wetting) according to the contact angle. A wetted droplet is identified as having an inner solid-liquid contact angle measuring less than 90°, whereas a non-wetted droplet has an angle measuring greater than 90° [55]. Surface tension is present between each interface of this solid-liquid-vapor system which defines the droplets wetting state. Thomas Young [74] found a relation between the surface tension and wettability of a system by an equilibrium of forces at the contact point (represented in Fig. 1.1), resulting in Young's equation

$$\gamma_{sv} = \gamma_{sl} + \gamma_{lv}\cos(\theta), \tag{1.1}$$

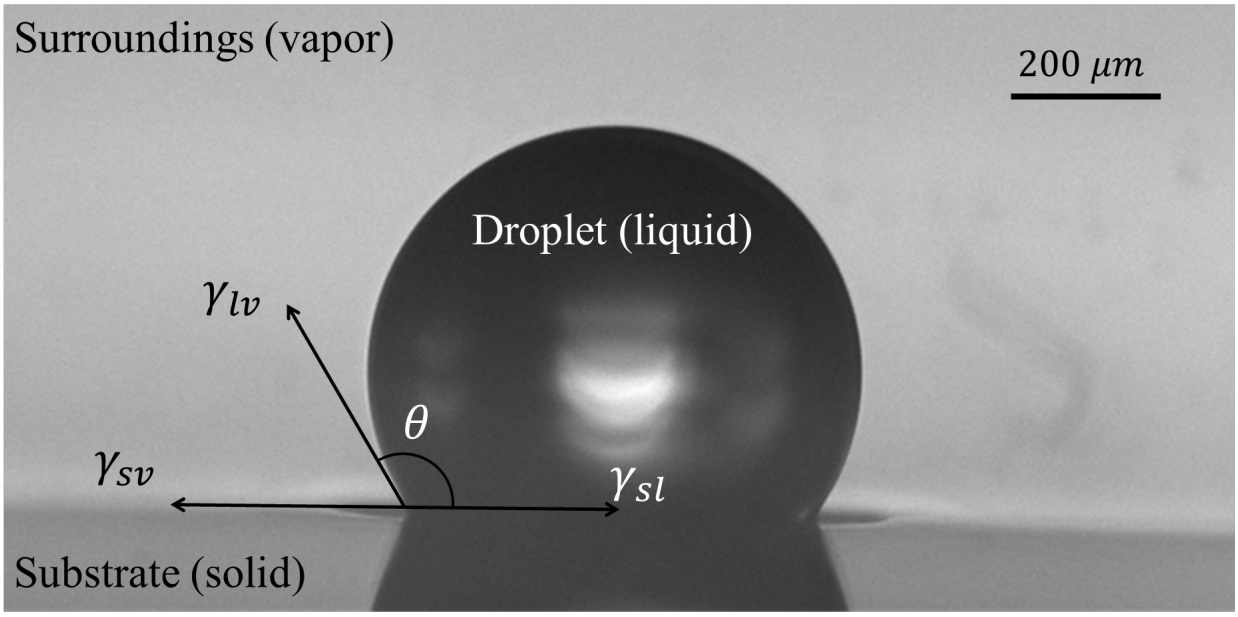

Figure 1.1: A representation of the direction of the surface tension forces, γ_{sv}, γ_{sl}, and γ_{lv} for sessile microdroplet with an equilibrium contact angle, θ. *Image Details*: Water droplet on acrylic polymer substrate with $T_s \cong 20$℃, $R \cong 276\mu m, \theta \cong 122^{\circ}$, $\forbar{V} \cong 122$ nL)

where θ is the contact angle and γ_{sv}, γ_{sl}, and γ_{lv} represent the solid-vapor, solid-liquid, and liquid-vapor surface tensions respectively. As seen in Eq. (1.1), the wettability of the droplet is dependent on all three phases of the system. This restricts the wettability of a solid-liquid-vapor system to remain constant under identical conditions. Unfortunately, experimental studies show this is not the case [47, 70].

Contact angle hysteresis (CAH) might help explain this discrepancy, which is dependent on droplet volume size, surface roughness, chemical attributes, and surface imperfections which are present in all real surfaces [23, 26, 32, 39, 71]. CAH is defined as the difference between the contact angle of an advancing and receding contact line (θ_a and θ_r respectively). There exist metastable states during the transition between an advancing-receding contact line, such that the contact line is fixed/pinned. This results in a range of intermediate contact angles, $\theta_r < \theta < \theta_a$, that the droplet will experience during a transition [18].

Substantial work toward identifying how the surface effects the droplet shape resulted in

two popular equations presented by Wenzel [73] and Cassie [11],

$$\cos\theta_{rough} = \eta\cos\theta_{smooth}, \tag{1.2}$$

$$\cos\theta_E = A_{f_1}\cos\theta_{Y1} + A_{f_2}\cos\theta_{Y2}, \tag{1.3}$$

which relate the wetting area to the wettability. Wenzel's equation (Eq. (1.2)) is a relation between the contact angle expected on an ideal surface (θ_{smooth}) and the observed angle (θ_{rough}) by the roughness of the surface (η). Cassie's equation (Eq. (1.3)) describes the effective contact angle, θ_E, for chemically patterned surfaces, Y_1 and Y_2, by the fraction of total surface area of each chemical, A_{f_1} and A_{f_2}. Recently, the accuracy of these equations has come into question, especially in the field of superhydrophobicity and nano-structured surfaces. For example, it was recently determined that the wettability of a liquid drop on a surface is solely dependent on the contact line, versus the entire contact area [28]. It was determined that Wenzel and Cassie equations are highly circumstantial [25, 40, 51], rather than incorrect.

1.1.2 Droplet Evaporation

In the transition from liquid to vapor, a droplet may experience a variety of modes that are dependent on surface temperature (depicted in Fig. 1.2). These modes include evaporation (Region I), nucleate boiling (Region II), and film boiling (Region IV), with an unstable transition region (Region III). A maximum heat flux is achieved such that an increase in surface temperature decreases the heat flux. This point is termed the critical heat flux (CHF), and represented in Fig. 1.2. Although all boiling regimes (Regions II - IV) are beyond the scope of this thesis, evaporation (Region I) provides the fundamental theory needed for such studies.

Much like a temperature gradient acts as a driving potential for heat transfer, a concentra-

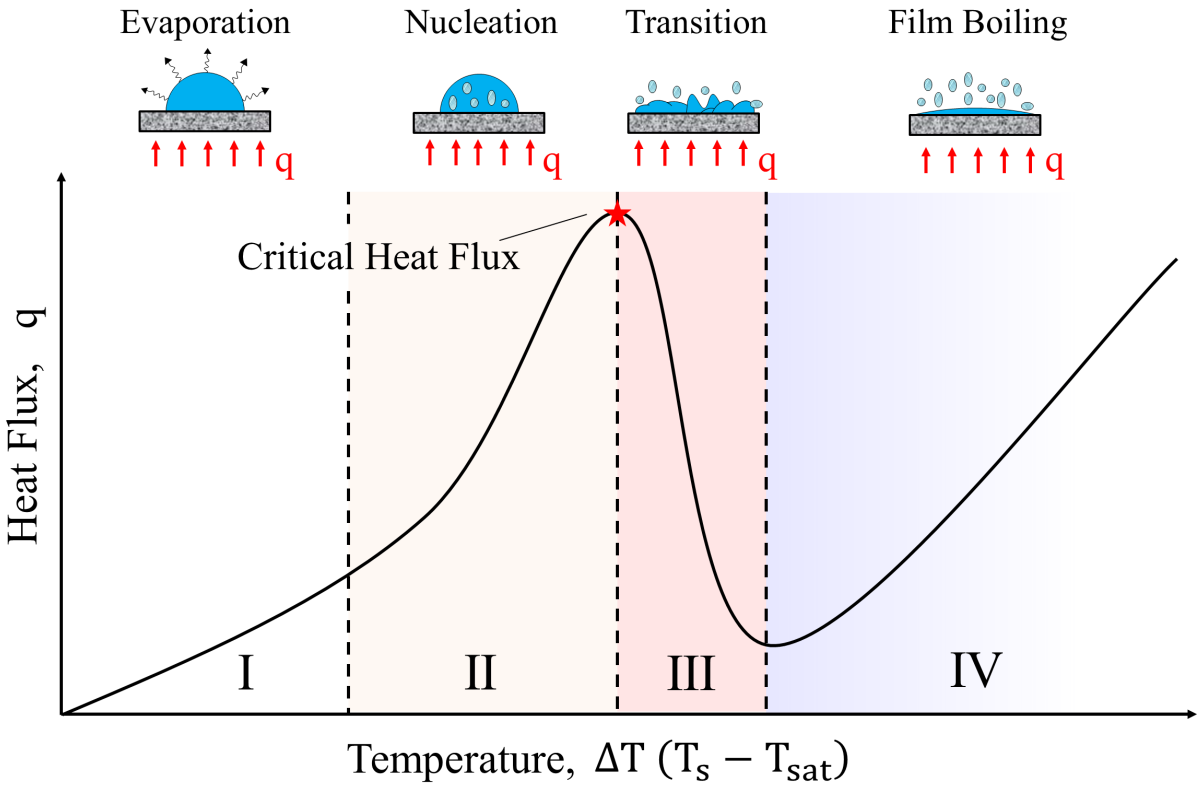

Figure 1.2: A typical boiling curve demonstrating the ability of various boiling regimes to remove heat flux.

tion gradient is a driving potential for mass transfer (evaporation) [3]. Droplet evaporation (mass transfer of vapor) will occur in the direction of high concentration (liquid droplet) to low concentration (surrounding environment) to achieve equilibrium. This vapor concentration surrounding the droplet is governed by Ficks law of diffusion, discussed in Section 3.1.1.

Modes of Droplet Evaporation

The rate of evaporation is strongly dependent on the contact line [15, 52, 65]. A larger contact area (i.e. longer contact line) has shown to give higher rates of evaporation. This explains the faster rates of evaporation experienced when the contact line remains fixed/pinned.

Therefore, accurately tracking the motion of the contact line is crucial for predicting the evaporation rate. In general, a droplet will experience one of three identified modes of evaporation, including (1) a constant contact radius mode (CCR), where the contact line is fixed or 'pinned' with a varying contact angle; (2) a constant contact angle mode (CCA), where the contact line is in motion with a decreasing contact radius while the contact angle remains constant; and (3) a mixed mode, where the drop experiences both a receding contact radius and contact angle [6]. Figure 1.3 demonstrates the change in volume of a droplet during CCA (Fig. 1.3a) and CCR (Fig. 1.3b) modes of evaporation. A fourth mode is occasionally used to describe contact line dynamics during an interchanging pinning (stick) and depinning (slip) contact line. This mode is termed 'stick-slip'. The transition between each mode is best predicted through the theory of contact angle hysteresis (CAH). A droplet has a contact angle during the advancement (increasing) of the contact line, θ_a. This provides an upper bound for an observed contact angle. Similarly, a lower bound is provided by a receding contact line, θ_r. Therefore, is can be estimated that the contact line will remain pinned during the transition between an advancing contact line, and a receding one ($\theta_r < \theta < \theta_a$) [18]. Similarly, a droplet is expected to maintain a constant contact angle during the advancing (during droplet formation) and receding (latter stages of evaporation) contact line.

Self-Cooling Effects

The rate of evaporation is dependent on the concentration of vapor at (1) the liquid-vapor interface and (2) the ambient surroundings (i.e. Ficks law of diffusion). The vapor concentration of the ambient surroundings is commonly discussed as the relative humidity, H (the ratio of ambient concentration to the saturated vapor concentration at the ambient temperature). The molecules along the liquid-vapor interface are considered saturated. The saturated vapor concentration is related to pressure and temperature by the Clausius-

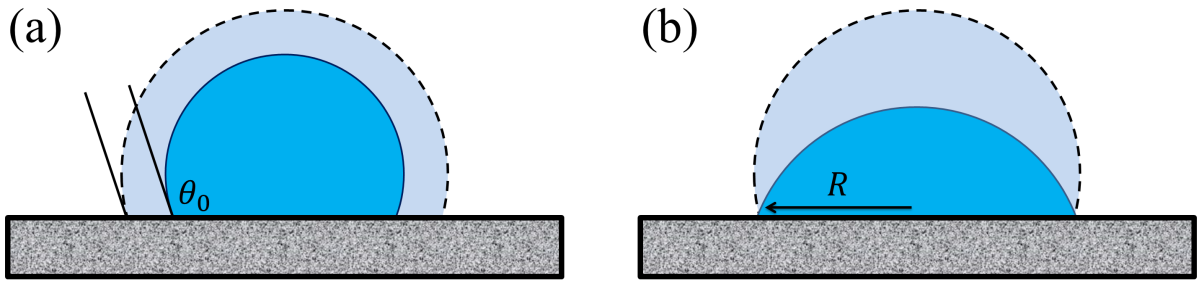

Figure 1.3: Volume evolution of a droplet experiencing (a) CCA mode of evaporation (b) CCR mode of evaporation. The CCR mode of evaporation (pinned contact line) will experience a net outward directed flow toward the contact line, whereas a net inward flow toward the center line for a de-pinned or a CCA mode of evaporation. [10]. This is due to the need for mass to be replenished at the contact line, which will otherwise be removed during evaporation with a receding contact line.

Clapeyron equation,

$$\ln\left(\frac{\mathbb{P}}{\mathbb{P}_{ref}}\right) = -\frac{\mathfrak{M}\Lambda_{lv}}{\Re}\left(\frac{1}{T} - \frac{1}{T_{ref}}\right), \tag{1.4}$$

coupled with the ideal gas law. $\mathfrak{M}$ is the molar mass (in this case, of water), $\Re$ is the universal gas constant, and Λ_{lv} is the latent heat of vaporization. The subscript '*ref*' refers to a known reference state.

Droplet evaporation is coupled with a decrease in droplet temperature [7, 8, 16, 38, 69], known as 'evaporative cooling.' The thermal resistance of the droplet causes an influence on the heat flux through the droplet, forming a temperature distribution. This cooling effect is more influential for larger droplets (larger liquid-vapor surface area), causing a larger temperature gradient due to the increased thermal resistance [16, 58]. Additionally, reports of a decrease in substrate temperature and inner fluid circulation patterns are induced [31, 34, 35, 41].

1.2 Direction of Research

A few of the basic theories of microdroplet evaporation have been presented, as further discussion increases the complexity far beyond the scope of this thesis. Significant progress has been made throughout the years toward understanding and predicting this phenomenon, although the depth of understanding remains very limiting.

In the previous discussion, droplet evaporation can be described by the dynamics of the contact line. CCR and CCA modes of evaporation allow simple models to account for the contact radius and contact angle dependence on evaporation to be modeled. It is important to note that both CCA and CCR modes are simply approximations, which gives the mixed mode as the only true mode experienced by an evaporating drop. Most of the published literature only considers mixed mode of evaporation when absolutely necessary (i.e. deviation from the other modes are too great). These inaccuracies will lead to higher evaporation rates for the CCR mode of evaporation assumption, or lower evaporation rates for CCA mode of evaporation assumption. These overlooked errors between theoretical results and experimental data poses issues in attempts to further predict the dynamics of droplet evaporation.

Research throughout the field have studied the dynamics of evaporation and put fourth attempts to validating numerical predictions under the naturally occurred modes. Methods of creating an evaporating drop experiencing *true* CCR are essential toward confirming the accuracy of the numerical solutions. Additionally, studies of a true CCR mode of evaporation allow accurate conclusions to be made on the theorized contact line dependence on evaporative heat transfer. This work focuses on two aspects of droplet evaporation; (1) experimentally controlling the contact line dynamics (a *forced* pinned contact line) during evaporation and (2) simulating numerical models to compare/validate with experimental data. To do this, a method of substrate fabrication is discussed, creating a circular "moat-

like" trench which refrains further advancement the contact line. This method of substrate fabrication (1) creates a pre-known surface area during droplet evaporation, (2) forces the contact line to remain pinned during evaporation, and (3) allows experimental studies of contact angle dependence on droplet evaporation. A new technique for droplet formation is introduced, using a fluid channel within the substrate to facilitate a 'bottom-up' method, which (1) allows a method for well controlled droplet formation and (2) introduces a setup for 'first time' steady state microdroplet evaporation studies. The experimental data is then compared to numerical models which assume a pinned contact line. A modification to the implemented numerical model is presented, to provide a better fit of the experimental data. This modification, which considers an imposed temperature/vapor concentration distribution along the liquid-vapor interface, provides a better fit for the experiential data. Thus, validation of the self cooling effects (termed 'evaporative cooling') during evaporation, and its contribution to microdroplet evaporation are made.

CHAPTER 2: LITERARY REVIEW

Droplet evaporation has been studied for over 100 years [24, 42]. Within this time, a wide range of experimental setups have been explored. As time progressed, theoretical models have become more sophisticated in attempts to understand/predict this process. This has led to hundreds of publications on droplet evaporation, comparing droplet size, liquid properties, substrate thermal conductivity, and substrate temperatures to name a few.

2.1 Constant Substrate Temperature

The most common model of droplet evaporation is a sessile droplet placed on a substrate maintained at a constant temperature. As previously mentioned, the self-cooling effect (evaporative cooling) during droplet evaporation causes a decrease in evaporation rate. The substrates ability to replenish this bulk temperature loss is dependent on the thermal properties of the substrate [17, 38]. Lopes et al. [38] compared numerical and experimental results of droplet evaporation on silicon (high thermal conductivity) and glass (low thermal conductivity). A 10% increase in total evaporation rate was reported for the silicon substrate. This result can be explained by the results from David et al. [17]. David et al. placed a thermocouple at various locations (both inside and outside) an evaporating sessile droplet. Low thermal conductivity surfaces (PTFE and Macor) showed ~ 1.5℃ decrease in the bulk droplet temperature. No temperature change in the droplet was observed for high thermal conductivity surfaces (Aluminum and Titanium). Therefore, it can be concluded that low thermal conductivity substrates are not able to distribute heat to the droplet as quickly as high thermal conductivity substrates, causing a local decrease in substrate temperature [17]. Thus, a constant substrate surface temperature is only possible (theoretically) when

the substrate has an infinite thermal conductivity [61, 69]. Although, a constant substrate temperature remains a safe approximation in the case of (1) a substrate with relatively high thermal conductivity (e.g., copper, silicone, and aluminum) and/or (2) the droplet size is significantly smaller than the substrate ($R_{drop} \ll R_{substrate}$) [15, 17, 46].

2.2 Modes of Evaporation

For droplets/substrates at room temperature ($T_s \approx 20$ ℃), microliter sized droplet lifetime is typically on the order of 10^3 seconds [5, 6, 16, 52]. The lifetime of nanoliter size droplets are expected to be an order of magnitude less [15, 50, 60]. A microdroplets *lifetime* is dependent on volume. Kelly-Zion et al. [36] found a volume dependence on *evaporation rate* when convection effects are considered. Convection effects were concluded to be negligible for contact radii $R \lesssim 4$ mm (i.e. negligible within the entire microdroplet regime). Additionally, contact radius near this scale will make the spherical cap approximation invalid ($R > l_c$ for water). The volume dependence on *evaporation rate* is therefore avoided within the water microdroplet regime. It has been reported that the evaporation rate is dictated by the contact line (solid-liquid-vapor interface) [15, 57, 58]. With this, tracking and predicting the motion of the contact line will provide insight on key factors effecting microdroplet evaporation.

2.2.1 Constant Contact Radius

As mentioned, the evaporation rate is dependent on the contact line (solid-liquid interface). Therefore, it should be intuitive that a droplet evaporating with a CCR (constant contact line length) will have a shorter lifetime than a droplet experiencing CCA mode of evaporation (a decreasing contact line length) [1, 5, 13, 15, 17, 46, 48, 52, 57, 61, 65, 69, 75].

T. Nguyen and A. Nguyen [49] studied droplet evaporation containing nanoparticles. An

increase in evaporation rate was reported with increasing nanoparticle concentration, while the initial equilibrium contact angle remained unaffected. A similar study using surfactants was done by Chandra et al. [13]. Chandra et al. came to the same conclusion, an increase in surfactant concentration causes an increase in (1) evaporation rate and (2) longer CCR mode of evaporation. Unlike T. Nguyen and A. Nguyen, Chandra et al. reported a decrease in initial contact angle (increase in initial contact radius) with increasing surfactant concentration. With recent findings on (1) contact line dependence on evaporation [15, 52, 57, 65] and (2) relations between pinning time and wettability [46, 57], the same conclusions can be made if no surfactants were present. Although, the presence of surfactants/nanoparticles are known to induce a CCR due to formation of the coffee ring effect [19, 20, 54].

The CCR mode of evaporation allows a method for studying the contact angle dependence on evaporation. Similar conclusions have been reported discussing the evolution of contact angle and droplet volume during evaporation with a CCR [1, 16, 29, 33, 44, 45, 63, 66], although contact line depinning mechanisms remain unclear. Sobac and Burtin [66] reported a linear volume evolution during CCR mode of evaporation for contact angles $\theta \lesssim 40°$. As a transition from non-linear to linear evaporation rate is difficult to depict, there is some discrepancy at this defining transition point (i.e. $\theta \lesssim 70°$ in Ref. [29]). Linear approximation models are available [33, 63], predicting the volume evolution and droplet lifetime with initial contact angles of $\theta < 90°$. Schönfeld et al. [63] provided a non-linear model showing the volume evolution follows $t \propto \mathcal{V}^{2/3}$. Deegan et al. [20] reported the evaporation rate proportional to the surface area ($\dot{m}_{lv} \propto R^2$), provided the evaporation flux is uniform along the liquid-vapor interface. The lack of a well-controlled pinned contact line causes conflicting conclusions.

2.2.2 Constant Contact Angle

Correlations between pinning forces and substrate wettability have been reported [4, 57, 65]. While methods for increasing the pinning forces have been discussed [5, 46, 50], progress toward inducing CCA mode of evaporation has shown little success. Pittoni et al. [52] reported droplets experiencing CCA modes of evaporation on smooth, low surface energy substrates once the contact line depinned. The initial pinning time is due to the surface imperfections (exhibiting CAH). Local peaks denoting metastable contact angles are observed during the "freely" moving contact line during CCA mode of evaporation. These local peaks are also found in similar studies [44, 45], although were not discussed. McHale et al. [45] found pinning forces (i.e. the transition from CCR to CCA) to be significantly altered for hydrophobic substrates. Wetted droplets ($\theta < 90°$) were reported to experience CCR mode of evaporation, whereas non-wetted droplets ($\theta > 90°$) experienced a CCA mode of evaporation. Similarly, a pinned contact line was observed during the initial stage of evaporation regardless of initial contact angle. Pittoni et al. and McHale et al. both reported *nearly* linear decrease in contact radius and apex height during the stages of evaporation experiencing a CCA.

Dash and Garimella [16] discovered minimal pinning forces for a structured superhydrophobic substrate ($\theta \sim 160°$). Slight pinning times are present in smooth hydrophobic substrates ($\theta \sim 120°$), supporting the previous discussion on surface imperfections and wettability pinning forces [45, 52]. Dash and Garimella [16] provided a derivation of the volume and radius time evolution for a droplet evaporating with a CCA. The squared radius was found to be proportional to time ($R^2 \propto t$), supporting the discussion by McHale et al. [45]. With the non-uniform evaporation flux solution provided by Popov [54], the time evolution of volume was found to be $\forall^{2/3} \propto t$. This verifies the results provided by Pittoni et al. [52], and the discussion of the 'nearly linear' profile evolutions by McHale et al. [45].

2.2.3 Mixed Mode

Both CCR and CCA modes of evaporation are approximations. Therefore, the mixed mode of evaporation (involving a decreasing contact radius and contact angle) provides the best physical model of droplet evaporation. Early reports by Bourgés-Monnier and Shanahan [6] reported a common final stage of droplet evaporation, where height, radius, and contact angle decrease (i.e. mixed mode). This stage typically occurs at $t \gtrsim 90\%$ of the droplets lifetime [1, 6, 45, 48, 52], regardless of the initial evaporation modes experienced (i.e. CCR or CCA modes of evaporation). With a time dependence on both contact radius and contact angle, conclusions are not always presenting. It is believed, for this reason, that droplets experiencing mixed mode of evaporation is typically avoided and/or not discussed in detail [1, 6, 15, 38, 45, 48, 52]. To the authors' knowledge, methods for maintaining control of the contact line during a droplets entire lifetime have not been reported. Thus, mixed mode evaporation is inevitable.

2.3 Pinning Forces

Maintaining precise control on the motion of the triple line is not an easy task. Therefore, many have worked toward understanding the cause of the motion of the triple line in attempts to predict the depinning transition. Bormashenko et al. [5] compared the droplet evaporation rate effects on high energy substrates (stainless steel, and aluminum) to low energy substrates (various polymers). The high energy surfaces showed longer CCR mode of evaporation than the low energy surfaces, while having a lower average surface roughness. The high surface roughness of the polymer substrates was determined to cause a stick-slip mode which occupied a majority of the droplets lifetime. As also reported by Pittoni et al. [52], when the surface roughness becomes large enough, the capillary forces cannot overcome the frictional forces. The result is a CCR mode of evaporation for a majority of the droplets

lifetime. Anantharaju et al. [1] reported a relation between the observed stick-slip mode of evaporation (pinning/depinning contact line) and the spacing of pillar topology patterned on a substrate surface. Mollaret et al. [46] found high energy surfaces (aluminum) pinning forces increase with increasing temperatures. Low energy surfaces (PTFE) showed little temperature dependence on pinning force. Crafton et al. [15] reported the CCR mode of evaporation being volume dependent. This was claimed to be due to larger capillary forces in smaller droplets, therefore being more susceptible toward a retracting contact line. Blake and Coninck [4] discussed the correlation between pinning forces and wettability of the substrate. This is supported by work of Putnam et al. [57] and Mollaret et al. [46]. Hydrophilic surfaces require the greatest depinning force, which decreases as the surface becomes more hydrophobic [4, 57]. This explains why superhydrophobic surfaces typically experience CCA mode of evaporation [1, 16, 65], although not exclusively [29, 44].

2.4 Solutions for Evaporation Flux

The process of droplet evaporation is limited by (1) the diffusion transfer across the liquid-vapor interface or (2) the diffusion relaxation of the immediate surroundings. Diffusion relaxation results in a solution of a uniform evaporation flux, whereas the diffusion transfer across the liquid-vapor interface gives a non-uniform solution [20]. The uniform flux provides a simple analytical solution [45, 60], although recent studies found this, is most cases, to be incorrect [20, 33, 54, 64].

2.4.1 Uniform Local Evaporation Flux

Early studies on droplet evaporation were presented with having a uniform evaporation flux [45, 60, 75]. This assumption lead to a simple analytical solution for the total evaporation rate. McHale et al. [45] has found this model to be semiempirical with $dR/dt \ll d\theta/dt$, giving

an overprediction for the surface area at which diffusion occurs. Yu et al. [75] provided an experimental study with comparisons to a fitted solution provided by McHale et al. [44]. The results showed an increasing error up to 7% as time increases, which confirms the over approximation initially reported by McHale et al [45]. It was found, however, that the evaporation flux is uniform for a contact angle $\theta = 90°$, regardless of the evaporation flux model (uniform or non-uniform evaporation flux) used [19, 20].

2.4.2 Non-Uniform Local Evaporation Flux

Recent studies worked on finding the evaporation flux valid for all contact angles. Deegan et al. [19, 20] discovered the evaporation flux of a sessile droplet is equivalent to the electrostatic field produced by a charged conductor, presented by Lebedev [37]. The resulting equation is given in Eq. (3.9) with the derivation detailed in Section 3.1.1. The solution gives a non-uniform evaporation flux along the droplets surface area for contact angles $\theta \neq 90°$ [20, 33, 41, 54]. The evaporation flux, J, was found to diverge at the contact line for contact angles $\theta < 90°$, yet converge to $J = 0$ for contact angles $\theta > 90°$ (refer to Fig. 3.2). With the solution of the local evaporation flux provided by Deegan et al. [19, 20], Popov [54] provided an exact solution for the total mass loss of an evaporating droplet. Although these solutions are widely discussed, many have resorted to applying simplified models to obtain analytical expressions.

Hu and Larson [33] reported a model for the evaporation flux acceptable for all contact angles between $0° < \theta < 90°$. Exact solutions were found when $\theta = 0°$ and $\theta = 90°$. This solution was later analyzed by T. Nguyen and A. Nguyen [50]. While proposing a corrected model, T. Nguyen and A. Nguyen further explaining the error associated with predicting a droplets lifetime when contact angles are larger than 90°. Other models were formulated with the assumption of either (1) a pinned contact line [30, 33, 41], or (2) free contact line motion with constant contact angle [41, 54] (i.e. CCR and CCA modes of evaporation respectively.)

However, the most common numerical solution (and in *most* cases, more meaningful) is the integration of the evaporation flux to provide the rate of mass lost due to evaporation [16, 20, 29, 41, 54]. These models stem from the solution provided by Popov [54].

CHAPTER 3: METHODOLOGY

3.1 Numerical Methods

3.1.1 Formulation of Laplace Equation

In the presented numerical model, the limiting rate of mass transfer is by diffusion at the liquid-vapor interface. With this, the evaporation of a microdroplet is governed by Fick's law of diffusion,

$$\frac{\partial c}{\partial t} = D\nabla^2 c, \tag{3.1}$$

where the diffusion constant, D, is assumed to be a constant. A quasi-steady state assumption is applied when the droplet lifetime, τ_E, is much larger than $D/{R_c}^2$ (i.e. $\tau_E \gg D/{R_c}^2$, where $D/{R_c}^2$ is known as the mass transfer Fourier number). In this case, the transient term in Eq. (3.1) is zero, resulting in the Laplace equation,

$$\nabla^2 c = 0. \tag{3.2}$$

The boundary conditions to satisfy the Laplace equation for an evaporating droplet are (1) the surface concentration (c_s - the vapor concentration at the liquid-vapor interface) is equal to the saturated vapor concentration, (2) the vapor concentration far from the droplet approaches ambient conditions (c_∞), and (3) all vapor flux occurs at the liquid-vapor interface. The local diffusion flux along the liquid-vapor interface is given by integrating over the entire liquid-vapor surface/interface

$$J(r) = -D\nabla c. \tag{3.3}$$

The flux is negative during evaporation due to the net mass flux out of the droplet. The total evaporation flux can therefore be calculated by

$$J_T = \int_{S_{lv}} J(r,t) \cdot \hat{n} dS, \tag{3.4}$$

where S the surface area where diffusion occurs (i.e. the surface area of the liquid-vapor interface) and $\hat{n}$ is the normal to the surface area.

This formulated Laplace equation with appropriate boundary conditions is identical to the solution of an electrostatic field due to a spherical cap conductor derived by Lebedev [37]. It is necessary to transform the droplet profile from cylindrical coordinates (r, z, ϕ) to toroidal coordinates (α, β, ϕ) for this case. The relation between the two coordinate systems are

$$r = \frac{R \sinh \alpha}{\cosh \alpha - \cos \beta}, \tag{3.5}$$

$$z = \frac{R \sin \beta}{\cosh \alpha - \cos \beta}, \tag{3.6}$$

where the azimuthal angle (ϕ) has the same meaning in both coordinate systems. Figure 3.1 provides a visual aid demonstrating the toroidal coordinate system (α, β, ϕ) for a sessile droplet in relation to the commonly implemented cylindrical coordinate (r, z, ϕ) system.

The solution of the Laplace equation given by Lebedev [37], in terms of vapor concentration is

$$\frac{c(\alpha,\beta) - c_\infty}{c_s - c_\infty} = \sqrt{2\cosh\alpha - 2\cos\beta} \times \int_0^\infty \frac{\cosh(\theta\tau)\cosh(2\pi - \beta)\tau}{\cosh(\pi\tau)\cosh(\pi - \beta)\tau} P_{1/2+i\tau}(\cosh\alpha) d\tau, \tag{3.7}$$

where $P_{1/2+i\tau}(\cosh\alpha)$ is the Legendre function of complex fractional degree given by

$$P_{-1/2+i\tau}(\cosh\alpha) = \frac{2}{\pi}\coth(\pi\tau) \times \int_\alpha^\infty \frac{\sin(\tau\xi)}{\sqrt{2\cosh\xi - 2\cosh\alpha}} d\xi. \tag{3.8}$$

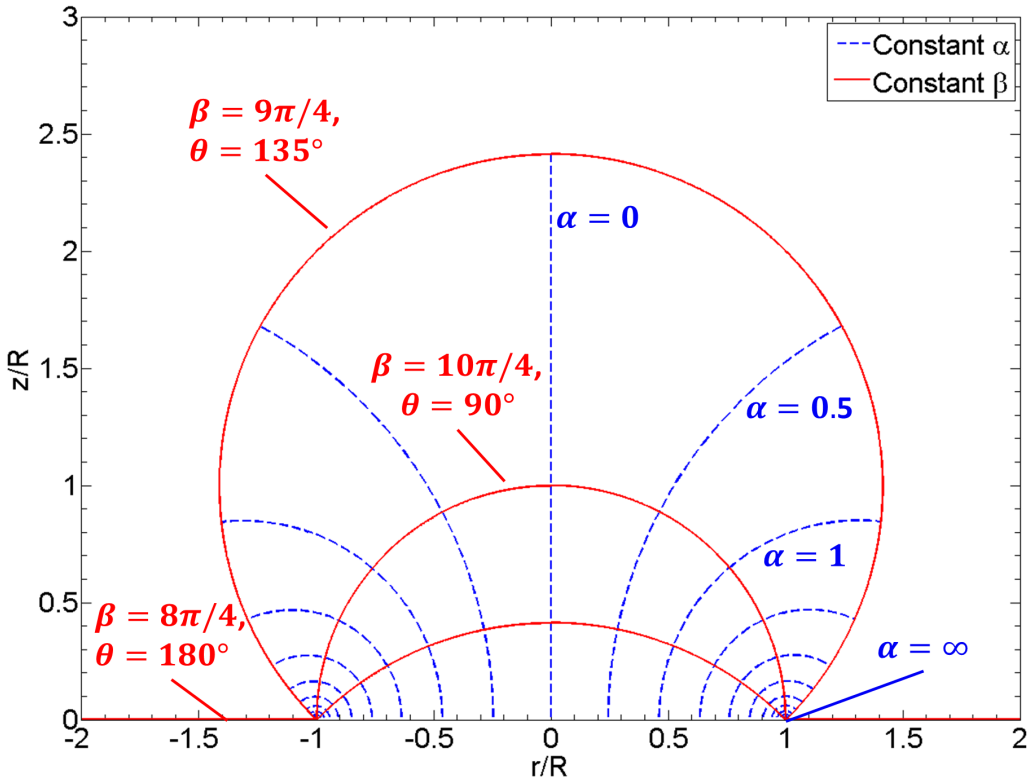

Figure 3.1: A 2D plot demonstrating the toroidal coordinate system (α, β) in a sessile droplet of contact radius R and its relation to the commonly known cylindrical coordinate system (r,z). The blue lines represent lines of constant α with a step size of 0.5 units. The red lines represent lines of constant β (step size of $\pi/4$). The contact angle is related to β by $\beta = 3\pi - \theta$, which correspond the liquid-vapor interface of a sessile droplet with contact angles of $\theta = 45^{\circ}$, 90°, 135°, and 180°.

Substituting Eq. (3.7) into Eq. (3.3) gives the local evaporation flux

$$J(\alpha) = \frac{D(c_s - c_\infty)}{R}\left[\frac{1}{2}\sin\theta + \sqrt{2}(\cosh\alpha + \cos\theta)^{3/2} \times \int_0^\infty \frac{\cosh(\theta\tau)}{\cosh(\pi\tau)} \tanh\left[(\pi-\theta)\tau\right] P_{-1/2+i\tau}(\cosh\alpha)\tau d\tau\right]. \quad (3.9)$$

Equation (3.9) is termed 'Deegans model' and is frequently referenced throughout this thesis (as well as reported in many recent publications [16, 20, 33, 41, 48, 54]). While many report the evaporation flux as $J(r)$, the solutions are related by the coordinate transform provided

by Eq. (3.5). It can be seen that Eq. (3.9) is not a function of ϕ (azimuthal angle). This is expected because evaporation is an axisymmetric phenomenon with axisymmetric boundary conditions.

An integration of Eq. (3.9) over the liquid-vapor interface will result in the total rate of evaporation for a particular contact radius (R) and contact angle (θ).

$$\dot{m}_{lv} = -\int_{S_{lv}} J(\alpha)\sqrt{1+\big(\nabla h(r)\big)^2}\, r dr d\phi \tag{3.10}$$

An integral transform [54] simplifies the total mass loss to

$$\dot{m}_{lv} = -\pi R D(c_s - c_\infty)\left[\frac{\sin\theta}{1+\cos\theta} + 4\int_0^\infty \frac{1+\cosh 2\theta\tau}{\sinh 2\pi\tau}\tanh\big[(\pi-\theta)\tau\big]d\tau\right]. \tag{3.11}$$

Equation (3.11) is termed 'Popovs model' and is frequently referenced throughout this thesis.

The droplet profile during evaporation requires droplet parameters to be a function of time ($R = R(t)$ and $\theta = \theta(t)$), resulting in a differential equation with respect to time. For a pinned droplet, the contact radius remains constant (i.e. $R(t) = R_0$). Therefore, the rate of mass loss can be represented through the rate of change of the contact angle. By geometric relations of a spherical cap (see Eq. (3.15)), the evolution of the contact angle during evaporation of a pinned droplet can be represented as

$$\frac{d\theta}{dt} = \frac{-D(c_s - c_\infty)}{\rho R^2}\big(1+\cos\theta\big)^2\Big[\frac{\sin\theta}{1+\cos\theta} + 4\int_0^\infty \frac{1+\cosh 2\theta\tau}{\sinh 2\pi\tau}\tanh\big[(\pi-\theta)\tau\big]d\tau\Big]. \tag{3.12}$$

Similarly, $\theta(t) = \theta_0$ during a CCA mode of evaporation. The evaporation rate is modeled by the change in contact radius as

$$\frac{dR}{dt} = \frac{D(c_\infty - c_s)}{\rho R}\frac{\big(1+\cos\theta\big)^2}{2+\cos\theta}\left[\frac{1}{1+\cos\theta} + 4\int_0^\infty \frac{1+\cosh(2\theta\tau)}{\sin\theta\sinh(2\pi\tau)}\tanh\big[(\pi-\theta)\tau\big]d\tau\right]. \tag{3.13}$$

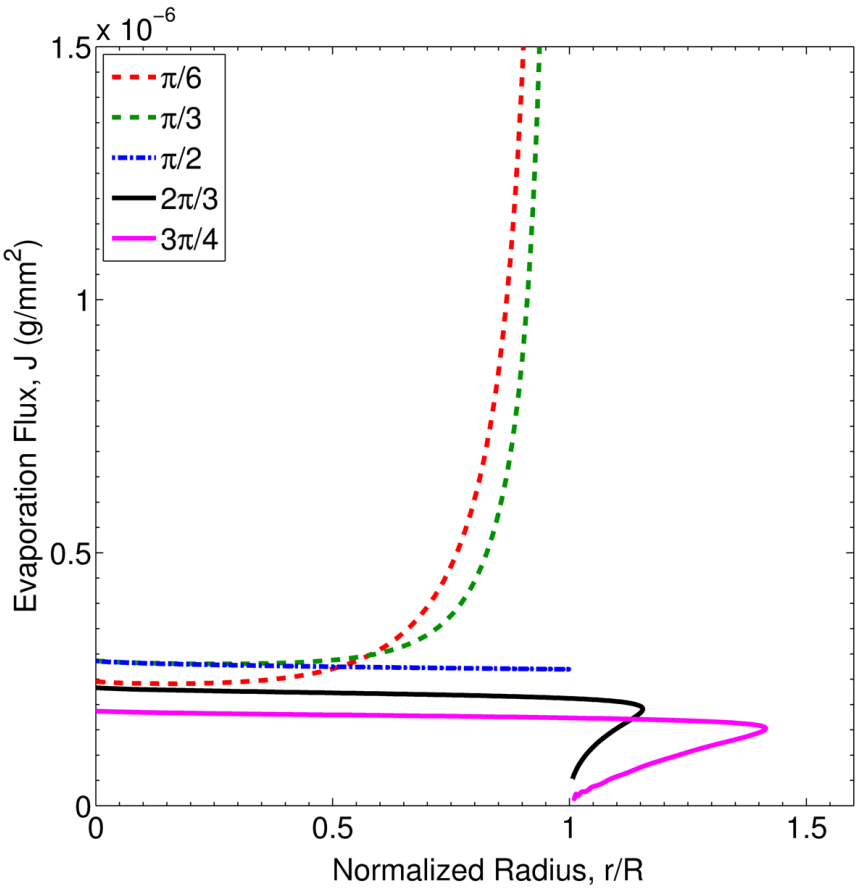

Figure 3.2: Plot representing the local evaporation flux, J, along the droplet surface area for various contact angles. The dashed lines are the solution for wetted droplets ($\theta < 90^{\circ}$), which diverge toward the contact line. The solid lines are the solution of non-wetted droplets ($\theta > 90^{\circ}$), and the dot-dashed line represents a uniform evaporation flux ($\theta = 90^{\circ}$). *Numerical data:* $D = 26.1\ mm^2, c_s = 1.83529\text{E–}8\ g/mm^3, c_\infty = 7.34116\text{E–}9\ g/mm^3$.

3.1.2 Numerical Evaluation for Evaporation Flux

The evaluation of the double integral in Eq. (3.9) (or the triple integral in Eq. (3.10)) is not trivial. While many provide a plot (similar to Fig. 3.2) demonstrating the numerical evaluation of Eq. (3.9) [16, 33, 41, 64], no information to the authors knowledge, is published explaining the numerical procedure for reproducing these plots. Therefore, this section is devoted to describing the numerical approach that was taken toward evaluating Eq. (3.9) for the local evaporation flux along the droplets liquid-vapor interface.

The toroidal coordinate α specifies a single point on the liquid-vapor interface. If α were to remain constant, an evaluation of Eq. (3.9) will provide the evaporation flux at this point (i.e. *local* evaporation flux). The evaluation of a multiple integral must be performed "inside-out" meaning, τ is constant as the Legendre function is integrated with respect to ξ. With this, integration can be performed on Eq. (3.8) by implementation of the trapezoidal rule [59] (more sophisticated numerical methods are not needed because the errors in the integration methods are far less than the errors in the theory itself).

The lower bounds are $\alpha = 0$ and $\tau = 0$ (i.e. the apex of the droplet, also see Fig. 3.1). Due to the hyperbolic cotangent term in Eq. (3.9), a singularity is presented when $\tau = 0$. Therefore, the first constraint is set such that $\tau > \epsilon$, where ϵ is some tolerance which is defined as $\epsilon = 10^{-4}$. Performing the trapezoidal rule to Eq. (3.8), a second constraint is found. A singularity is present when $\xi = \alpha$. Therefore, (as done with the lower bound for τ) the lower bound for ξ is set to $\xi - \alpha > \epsilon$. The evaluation of the Legendre function converged for $\alpha - \xi \cong 10$ (with step size of $\Delta\xi = 0.01$). The result is the modified Legendre function for integration.

$$P_{-1/2+i\tau}(\cosh\alpha) = \frac{2}{\pi}\coth(\pi\tau) \times \int_{\alpha+\epsilon}^{10-(\alpha+\epsilon)} \frac{\sin(\tau\xi)}{\sqrt{2\cosh\xi - 2\cosh\alpha}} d\xi, \quad \text{for } \tau > \epsilon \qquad (3.14)$$

The Legendre function in Eq. (3.9) is now single valued during implementation of the trapezoidal rule with respect to τ, and the only singularity present during the evaluation of Eq. (3.9) is the Legendre function at $\tau = 0$. The absolute maximum value of τ was found to be $\tau \approx 225$. This value of τ causes $\cosh(\pi\tau) \to 10^{308}$, which nears the maximum floating point. Although, the solution converges for $\tau \approx 10$ with sufficient accuracy when $\Delta\tau = 0.01$.

The solution of Eq. (3.9) is now set up to provide the evaporation flux at a single point along the droplets liquid-vapor interface/surface (α is single valued). The final step is to evaluate Eq. (3.9) across the entire liquid vapor interface ($0 \leq \alpha < \infty$). Convergence is

achieved for $\alpha \approx 5$ using $\Delta\alpha = 0.1$. A summary of the ranges of α, τ, and ξ for evaluating Eq. (3.9) are

$$J(\alpha) \begin{cases} 0 < \alpha \lesssim 5 & \Delta\alpha = 0.1, \\ \epsilon < \tau \lesssim 10 & \Delta\tau = 0.01, \\ \alpha + \epsilon < \xi \lesssim 10 - (\alpha + \epsilon) & \Delta\xi = 0.01. \end{cases}$$

The MATLAB code used to evaluate Eq. (3.9) is provided in Appendix A. The step by step evaluation helps identify acceptable lower and upper bounds to avoid long computation time and an ill-behaved function. The evaluation of Eq. (3.9) providing the evaporation flux along the droplets liquid vapor interface for various contact angles ($30° < \theta < 135°$) is represented in Fig. 3.2. This plot is similar to ones provided in a number of publications [16, 33, 41, 48, 64], confirming there are no errors in the code. It has been noticed that the provided results may lack clarity, diminishing its importance. Therefore, the evaporation flux is plotted in a vector notation (blue arrows, see Fig. 3.3) along the liquid-vapor interface (red curves, see Fig. 3.3) for a wetted droplet ($\theta = 45°$) and non-wetted droplet ($\theta = 135°$). Symbols in the plot are to act as guides for relating the evaporation flux plots (Figs. 3.3a and 3.3b) to the vector plots (Figs. 3.3c and 3.3d). For contact angles $\theta < 90°$, the evaporation flux diverges at the contact line. Contrary, for $\theta > 90°$, the evaporation flux converges to $J = 0$ at the contact line. Moreover, the evaporation flux is uniform along the entire liquid-vapor interface for $\theta = 90°$.

3.2 Experimental Setup

3.2.1 Substrate Fabrication

The substrates used in the experiments are clear acrylic polymer disks (1 in. diameter, 0.25 in. thickness). The method of droplet formation is by an inner fluid channel. Figure 3.4a shows a circular fluid channel drilled within the substrate ($\not{d} \approx 1.6$mm). A micro drillbit

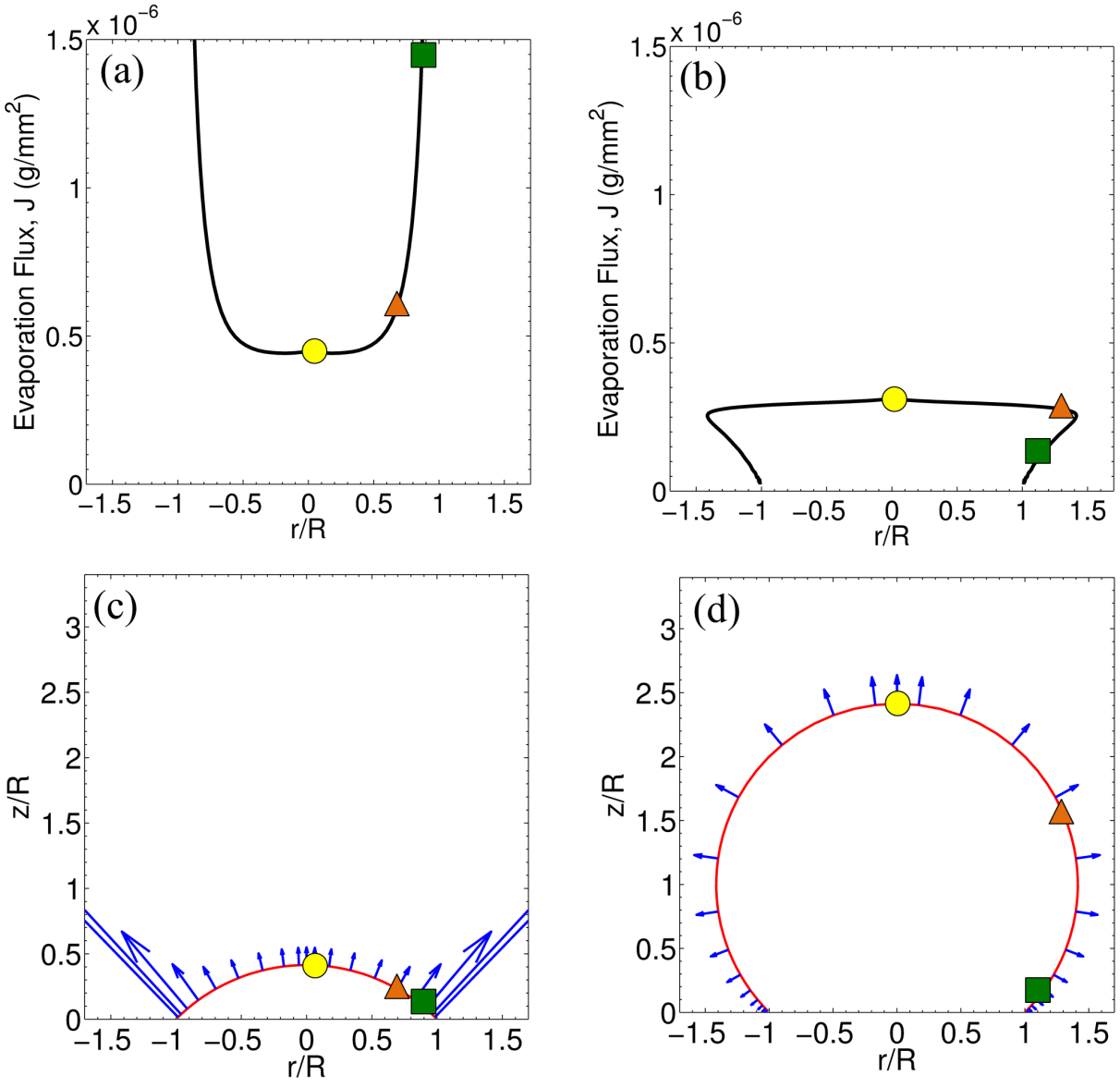

Figure 3.3: Plots representing the local evaporation flux, J, along the droplet surface area for contact angles of (a) $\theta = 45^{\circ}$ (hydrophilic) and (b) $\theta = 135^{\circ}$ (hydrophobic). The vector plot representation of the evaporation flux on a droplet surface are represented in (c) and (d), respectively. The vector plot provides a clear demonstration of the distinct difference in the evaporation flux solutions between wetting and non-wetting droplets. The symbols are included to provide a visual guide for relating the evaporation flux plots to vector plots. *Numerical data:* See Fig. 3.2.

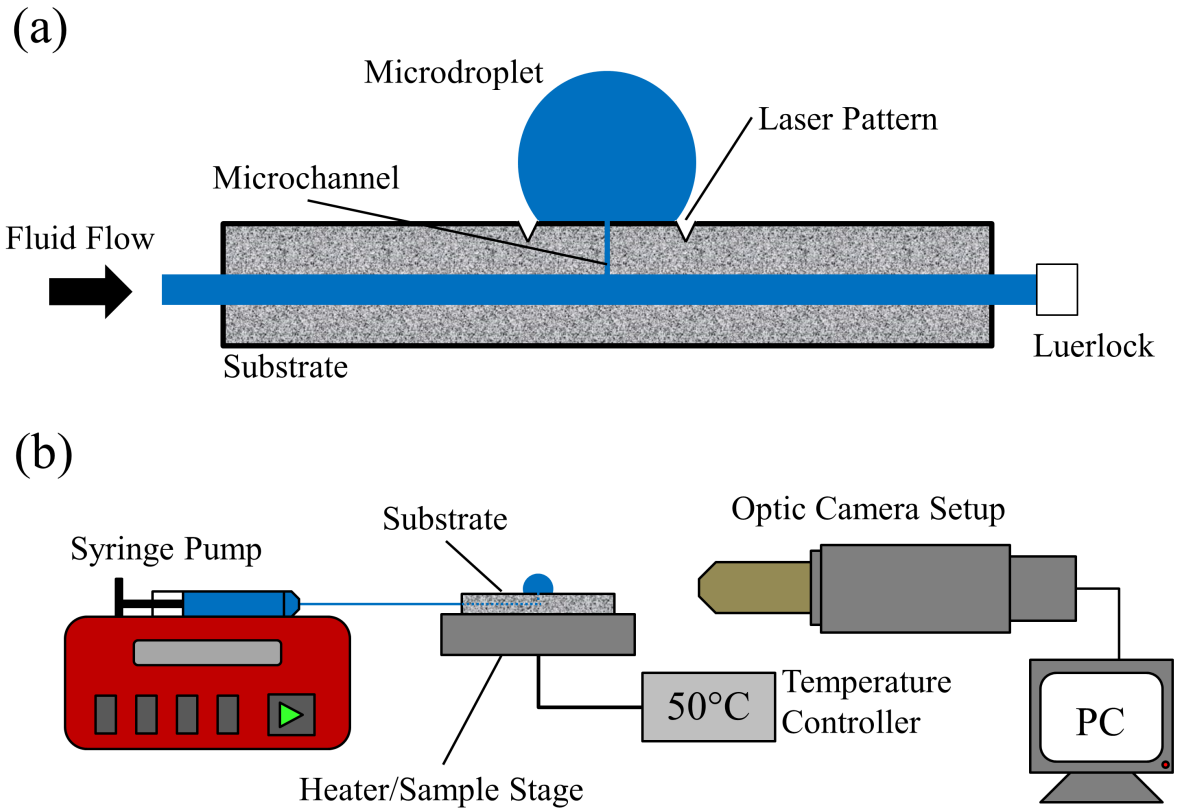

Figure 3.4: (a) Sample substrate with laser pattern and inner fluid channel supply. (b) Schematic of experimental setup for a 'force-fed' microdroplet evaporation.

($\not{d} = 200\mu$m) is used to drill a hole normal to the surface, intersecting the inner substrate channel near the center of the substrate. Prior to experiments, the substrate is cleaned with ethanol and dried with pressurized air to remove all debris.

A femtosecond laser (3 Watt Coherent Chameleon Ultra I) is used to create a circular pattern centered around the micro-drilled hole. This laser patterning process is based on ultra-short pulses acting as an intense heat source [72], allowing a direct solid-vapor transition (ablation) [14]. Prior to laser patterning, the substrate surface is colored with a black Sharpie® permanent marker. Once dried, a second layer of black Expo® dry erase marker is colored over the permanent marker layer. This combination of layer preparation facilitates heat absorption (using the dry erase marker) via the laser for the subsequent polymer sur-

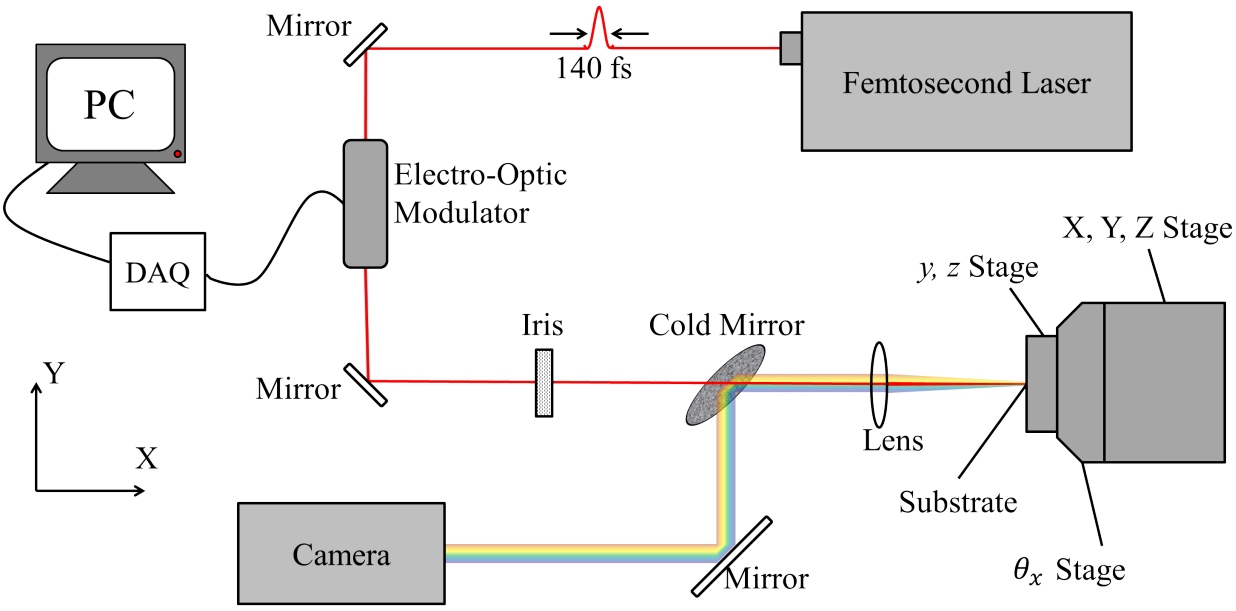

Figure 3.5: A simplified schematic of experimental setup used for laser patterning substrates.

face ablation, while refraining from affecting the surrounding non-targeted zone (using the permanent marker). The prepared substrate is placed on a six degree of freedom patterning stage (y, z, θ_x, X, Y, Z as shown in Fig. 3.5). For patterning the polymer substrates, the laser output parameters are a pulse width of 140 fs at 80MHz with a wavelength of $\lambda =$ 795nm and a steady state base power of $\sim$ 2 Watts. An Electro-Optic Modulator (EOM) is used to control of the pulse duration, where a user-defined voltage function output to a DAQ board controls the EOM. The sample is rotated manually at $\dot{\omega} \approx$ 12rpm during the ablation procedure. This procedure produces a pattern spot size of $d_p \approx 100\mu$m, with a penetration/ablation depth of $\delta_p \approx 50\mu$m.

3.2.2 Microdroplet Evaporation Measurements

For all experiments, 0.2μm filtered water is used as the working fluid. Prior to measurements, one end of the substrate channel is connected to a syringe pump (for supplying the water) and the other end of the fluid channel extends to a fluid dump. Water is continuously

pumped through the channel system into the fluid dump to remove any possible air bubbles trapped within the system during the initial setup. Once the air bubbles are removed, the syringe pump is stopped and a luer lock is used to seal the channel extending to the fluid dump (thus, directing the water to the substrate surface through the microchannel for forming droplets). A flow rate of 2 μL/min ($\approx$ 33 nL/s) is used for forming droplets within the patterned structure.

The substrate is placed on a custom electric $\sim$75Ω heater/sample stage. The substrate temperature is regulated with a temperature controller coupled to a K-type thermocouple. The sample stage temperature was calibrated with comparison to boiling water at 100℃, additional T-type thermocouple/multimeter measurements and standard thermometer measurements. The measurement error in temperature from the temperature controller and electric heater device is $T_s \pm 1.5$℃.

For video recordings, a CCD camera (Point Grey Flea3) is coupled with a visible achromatic eyepiece lens (f_{eye}= 200mm) and line-replaceable Mitutoyo long working distance microscope objectives (5$\times$ and 20$\times$). Video streaming is acquired at 20 fps with a CCD region-of-interest of 960$\times$540 pixels. The magnification of the 5$\times$ and 20$\times$ objectives provided image resolutions of $\sim$2.74 μm/pixel and $\sim$0.685 μm/pixel, respectively. A schematic of the experimental setup for data collection is shown in Fig. 3.4b.

A custom image analysis LabVIEW program facilitates data collection [57, 58]. The image analysis program continuously captures images from the CCD camera and analyzes the droplet through a greyscale edge-detection technique. The image analysis/acquisition program measures the contact radius R, contact angle θ, and apex height h by incorporating a spherical cap fit to the edge contour (see Fig. 3.6). The volume of the droplet is then calculated through a spherical cap relation.

$$\mathcal{V} = \frac{\pi R^3}{3\sin^3\theta}\left(2 - 3\cos\theta + \cos^3\theta\right) \tag{3.15}$$

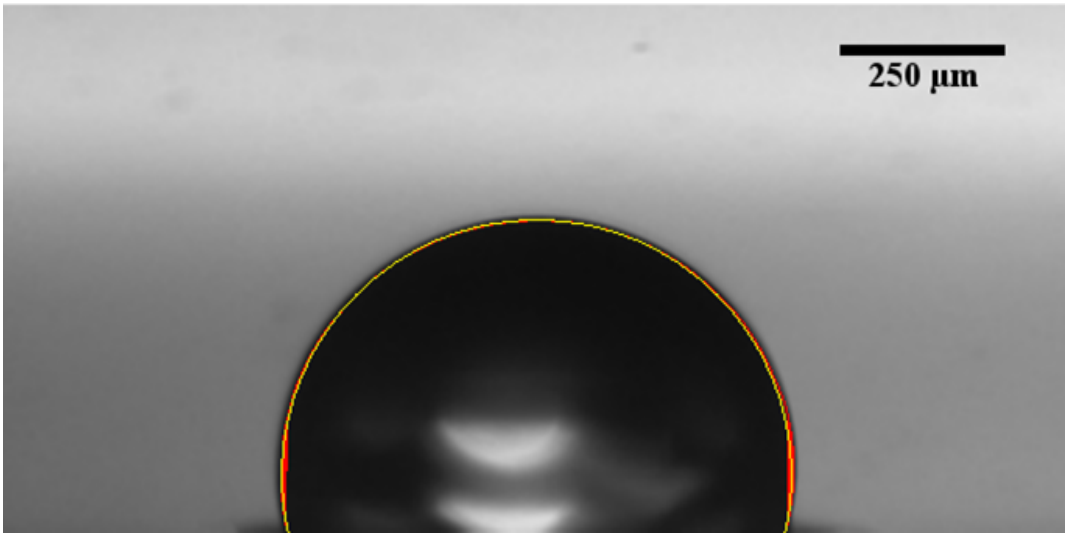

Figure 3.6: A sample of a trimmed image analyzed through a custom LabVIEW code. The red lines provide the edge contour, and the yellow line provides a best circular fit for the droplet. The droplet profiles are then found by measuring the radius, contact angle, and height of the circular fit line.

The proposed method for droplet formation does influence the evaporation rate slightly. For example, once the syringe pump is stopped, there is still fluid flow into the droplet due to the pressure buildup within the fluid channel leading to the droplet. This causes the measured evaporation rate to be slower than other reported values (see Fig. 8 in Ref. [57]). This error is minimized by evaluating numerical predictions using the measured step evolution of the droplets profile (i.e. R and θ), thus simulating an equivalent evaporation rate. Further confirmation of the error associated with the implemented fluid channel is through comparisons of droplet evaporation on (1) non patterned substrates and (2) manually placed onto the substrate (i.e. not implementing the inner substrate fluid channel, discussed in Section 4.2). It is concluded that the decreased evaporation rate due to the excess flow once the syringe pump has stopped is minimal, and remains within the error of measurements.

CHAPTER 4: EXPERIMENTAL RESULTS

4.1 Evaporation with Pinned Contact Line

The droplet profile is measured during evaporation on both (1) a laser patterned acrylic polymer substrate (Fig. 4.1c) and (2) a non-patterned acrylic polymer substrate (Fig. 4.1b). The laser patterned substrate classifies a *forced pinned* contact line due to the step edge pattern, whereas droplet evaporation remains unaffected (i.e. *naturally pinned*) on the non-patterned substrate. The droplet contact angle on the non-patterned substrate is predicted by Youngs' Equation. The equilibrium contact angle for the polymer substrate is $\theta \approx 72.8^{\circ} \pm 3^{\circ}$. Therefore, the contact radius is dependent on the infused volume for the non-patterned substrates. Due to forcing the contact line to be within the patterned section (for the patterned substrates), a contact angle can be achieved on patterned substrates such that $\theta > \theta_a$. The droplet remains within the laser patterned moat-like trench for $\theta \lesssim 120^{\circ}$. For $\theta > 120^{\circ}$, pinning forces are not enough to keep the droplet within the patterned region. Thus, for $\theta > 120^{\circ}$, the droplet contact line depins from the patterned section and is no longer effective at pinning the contact line. The maximum observed contact angle before depinning is $\theta_{max} \approx 1.5\theta_E$, allowing the formation of both wetted and non-wetted droplets under identical conditions.

For initial measurements, each substrate is heated to elevated temperatures of 50℃ and 65℃. An infuse rate of 2 μL/min ($\approx$ 33 nL/s) is used during the droplet formation. Data recordings are started automatically once the syringe pump has been stopped (through a custom LabVIEW program). Images are captured and analyzed every 0.25s (4 fps). The droplet parameters (R, θ, $\forbidden$, and h) are non-dimensionalized with respect to the initial

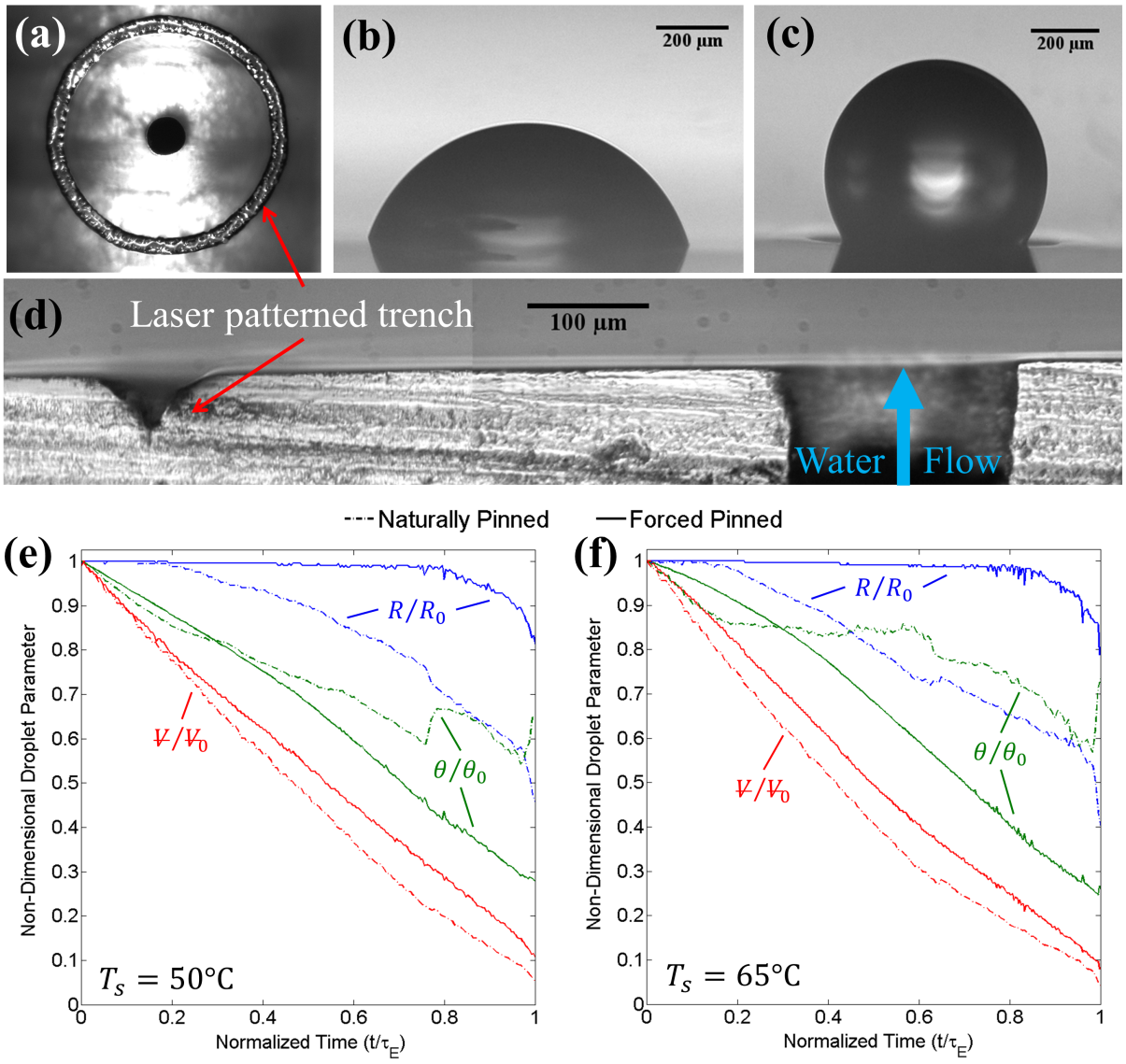

Figure 4.1: (a) A surface view and (d) a zoomed cut view of a laser patterned polymer substrate with a pattern radius $R_p \approx 500\mu$m is shown (fluid-flow channel $\forbar{d} \approx 200\mu$m, $\forbar{d}_p \approx 100\mu$m, $\delta_p \approx 50\mu$m). The effectiveness of the pattern to pin the contact line can be seen when comparing droplets (b) and (c) of similar volumes ($\forbar{V} = 122 \pm 1$ nL. An non-patterned polymer substrate is represented in (b), which demonstrates a naturally formed droplet with the equilibrium contact angle according to Youngs' equation ($R \cong 450\mu$m, $\theta \cong 72.6°$). A patterned substrate is represented in (c), which provides a method for forcing the contact line to be fixed and a contact angle $\theta > \theta_E$ ($R \cong 276\mu$m, $\theta \cong 122°$). The droplet profile during evaporation of (b) a naturally pinned droplet (dashed lines) and (c) a force pinned droplet (solid lines) with surface temperatures of $T_s = 50$℃ and $T_s = 65$℃ are shown in (e) and (f) respectively. It is important to note the dramatic increase in the contact line pinning time between the two substrates ($\sim 0.2\tau_E$ to $\sim 0.8\tau_E$) under otherwise identical conditions.

conditions (R_0, θ_0, ~~V_0~~, and h_0). Figures 4.1e and 4.1f provide plots of the dimensionless droplet-profile for both substrates (patterned and non-patterned) as a function of the droplet lifetime (t/τ_E) at $T_s = 50$℃ and $T_s = 65$℃, respectively. The image analysis software is terminated when the droplet becomes significantly small (due to increased error in the edge-finding software for droplet dimensions (i.e. R and h) comparable to five times the imaging resolution (e.g. $R \lesssim 5\mu$m and/or $h \lesssim 5\mu$m with the 20× objective)). As shown in Fig. 4.1, the patterned substrate is effective in controlling the contact line, where there are distinct differences between the plotted microdroplet parameters during evaporation on the non-patterned substrate (naturally pinned, represented by dashed lines) and the patterned substrate (forced pinned, represented by solid lines).

4.1.1 Naturally Pinned Droplet Evaporation

Droplet evaporation on a non-patterned substrate is shown in Fig. 4.2. The observed CCR mode of evaporation is represented by τ_P. Regardless of the surface temperature, the time at which the contact line naturally depins is $\tau_D \approx 0.2\tau_E$. This is supported by results by Mollaret et al. [46]. Once the contact line has depinned, the deviation between the two non-patterned cases increases significantly. For $T_s = 50$℃, the droplet has no distinct characteristics of evaporation for $0.2\tau_E \lesssim t \lesssim 0.75\tau_E$. This mode of evaporation is best classified as mixed mode. The contact line depinning in a stick-slip mode of evaporation can be seen at $\sim 0.75\tau_E$ and $\sim 0.95\tau_E$, where the contact angle experiences a spike increase. The minimum contact angle before the depinning for both data sets is $\theta_r \approx 44°$. Droplet evaporation at $T_s = 65$℃ experiences different characteristics. Once the contact line has depinned ($t \sim 0.2\tau_E$), the contact angle stays relatively constant until $t \sim 0.6\tau_E$. This region of evaporation can be *estimated* as CCA mode of evaporation. Preceding this second region of evaporation, no distinct characteristics are observed for $0.6\tau_E \lesssim t \lesssim 0.98\tau_E$. Near the end of the droplets lifetime, a large spike in the contact angle is seen at $\sim 0.98\tau_E$. This

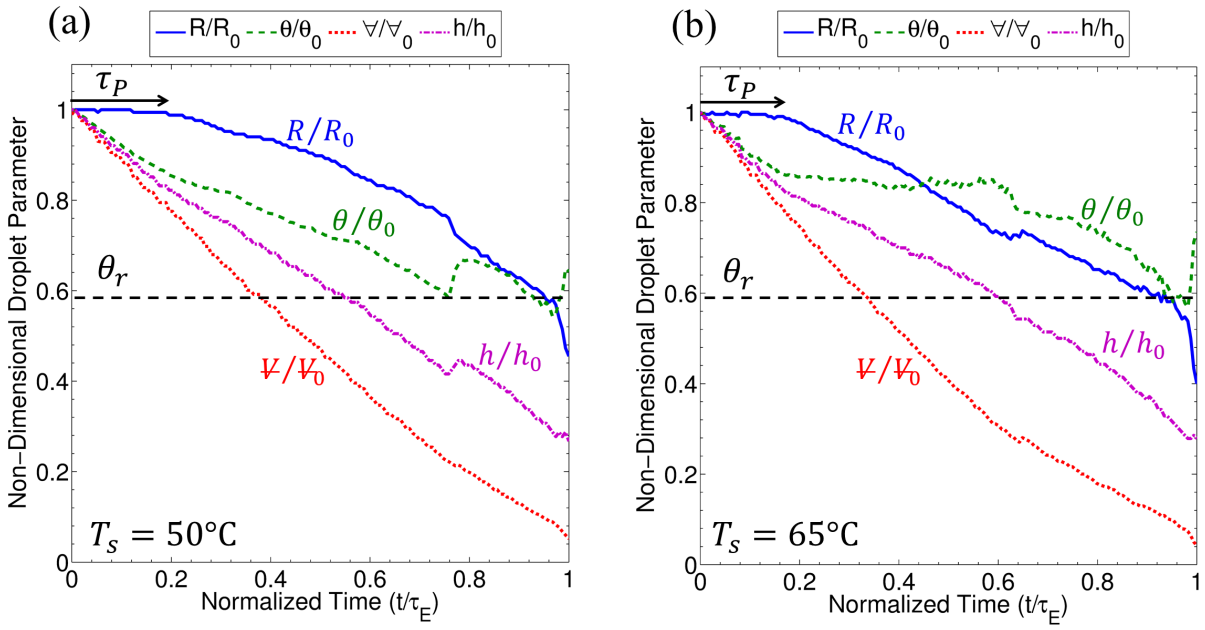

Figure 4.2: Droplet evaporation on an non-patterned polymer acrylic substrate at elevated surface temperatures of (a) $T_s = 50$℃ and (b) $T_s = 65$℃. The arrow represents the pinning time (τ_P, the duration of the CCR mode of evaporation), and a dashed line marks the receding contact angle (θ_r). The effect of surface temperature on droplet evaporation characteristics is evident once the contact line has depinned ($t \gtrsim 0.2\tau_E$). The depinning angle ($\theta_r \approx 44^\circ$) is found to be consistent between the two cases. *Experimental Data*: (a) $T_s = 50$℃, $R_0 \cong 460.9\mu$m, $\theta_0 \cong 62.9^\circ$, $\forall_0 \cong 104.4$ nL, $h_0 \cong 278.8\mu$m, $\tau_E \cong 38.25s$; (b) $T_s = 65$℃, $R_0 \cong 576.8\mu$m, $\theta_0 \cong 68.1^\circ$, $\forall_0 \cong 232.2$ nL, $h_0 \cong 380.9\mu$m, $\tau_E \cong 42.0s$.

is due to the contact angle $\theta = \theta_r$. Overall, there is an observable difference between droplet evaporation on a non-patterned substrate at different elevated surface temperatures. This is caused by the different time duration of each mode of evaporation (CCR, CCA, mixed mode, then stick-slip). Table 4.1 summarizes the transition time period between each mode of evaporation.

4.1.2 Forced Pinned Droplet Evaporation

Droplet profile data during evaporation on a patterned substrate of $R_p \approx 600\mu$m is shown in Fig. 4.3. The CCR mode of evaporation dominates the droplets lifetime ($\tau_P \approx 0.8\tau_E$) on the laser patterned substrate. As reported for the non-patterned substrate, the pinning time is not found to be dependent on surface temperature. Depinning occurs once the con-

Table 4.1: Summary of the time period associated with each observed mode of evaporation on a non-patterned substrate with respect to the droplets lifetime, τ_E.

	$T_s = 50$℃	$T_s = 65$℃
CCR	$t \lesssim 0.2\tau_E$	$t \lesssim 0.15\tau_E$
CCA	–	$0.15\tau_E \lesssim t \lesssim 0.6\tau_E$
Mixed	$0.2\tau_E \lesssim t \lesssim 0.75\tau_E$	$0.6\tau_E \lesssim t \lesssim 0.98\tau_E$
Stick-Slip	$t \gtrsim 0.75\tau_E$	$t \gtrsim 0.98\tau_E$

tact angle reaches $\theta \sim 35^\circ$, which is considerably less than the receding contact angle on the non-patterned substrate ($\theta \sim 44^\circ$). Once the contact line has depinned, the contact angle continues to decrease along with a decreasing radius. Therefore, the end of a forced pinned droplets lifetime ($t \gtrsim 0.8\tau_E$) is best classified as mixed mode of evaporation. Only two modes of evaporation are observed on the patterned substrate, compared to three or four which occurred on the naturally pinned substrate (depending on the substrate temperature). Moreover, the CCR mode of evaporation dominated ∼80% of the droplets lifetime. Thus, a forced pinned contact line on the laser patterned substrate simplifies the contact line dynamics during microdroplet evaporation. Unlike the non-patterned substrate, the droplet evaporation characteristics with a forced pinned contact line are consistent at both surface temperatures; thus facilitating improved experimental methods for predicting droplet evaporation with higher accuracy.

4.2 Contact Line Dependence on Evaporation Rate

While there are a substantial amount of reports demonstrating contact line dependence on evaporation rate [8, 46, 57], Dash and Garimella [16] found a contact angle dependence on hydrophobic surfaces ($\theta \gtrsim 110^\circ$). The solution of Deegans model supports this conclusion (see Fig. 3.3d). To test this contact angle dependence, a series of experiments are performed.

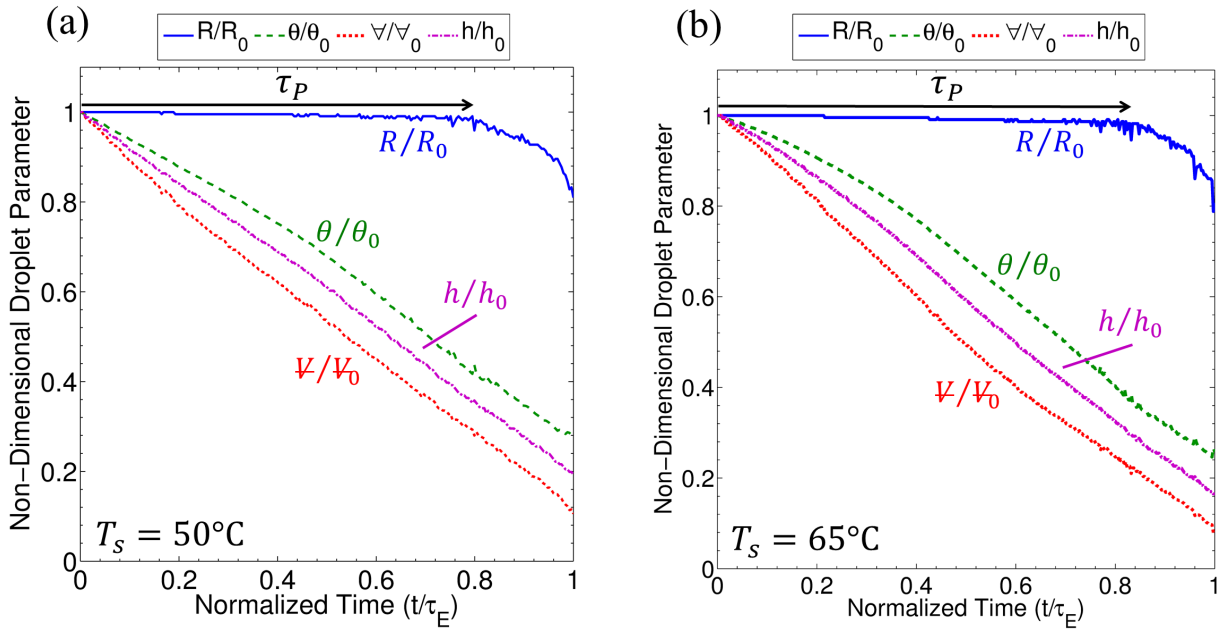

Figure 4.3: Droplet evaporation on a patterned polymer acrylic substrate at elevated surface temperatures of (a) $T_s = 50$℃ and (b) $T_s = 65$℃. The arrow represents the contact line pinning time (τ_P, the duration of the CCR mode of evaporation). The effectiveness of the patterned surface to pin the contact line is evident *Experimental Data*: (a) $T_s = 50$℃, $R_0 \cong 610.0\mu$m, $\theta_0 \cong 77.4^{\circ}$, $\forbidden_0 \cong 343.9$ nL, $h_0 \cong 485.8\mu$m, $\tau_E \cong 62.25s$; (b) $T_s = 65$℃, $R_0 \cong 612.7\mu$m, $\theta_0 \cong 87.6^{\circ}$, $\forbidden_0 \cong 449.0$ nL, $h_0 \cong 585.1\mu$m, $\tau_E \cong 93.75s$.

These experiments include measuring the evaporation rate of droplets on (1) non-patterned substrates (both manually placed from above, and using the described inner fluid channel), and (2) five patterned substrates ($R_P^{\mathrm{I}} \cong 260\mu$m, $R_P^{\mathrm{II}} \cong 380\mu$m, $R_P^{\mathrm{III}} \cong 450\mu$m, $R_P^{\mathrm{IV}} \cong 480\mu$m, and $R_P^{\mathrm{V}} \cong 600\mu$m). Both patterned and non-patterned substrates are used to facilitate experiments of hydrophilic (non-patterned) and hydrophobic (patterned) substrates. Specifically, the patterned substrates allow contact angles above 110° to compare with Dash and Garimella [16]. Additionally, the manually placed droplet methodology introduces a comparative study on microdroplet evaporation implementing the inner substrate fluid channel. These results are used to determine the magnitude at which the inner fluid channel effects a droplets evaporation rate. For all experiments conducted (at various substrate temperatures of $T_s = 21$℃, $T_s = 35$℃,$T_s = 50$℃, $T_s = 65$℃, and $T_s = 75$℃), the large range of initial

contact angles measured is $57^\circ < \theta_0 < 127^\circ$.

The evaporation rate ($\dot{m}_{lv}$) is measured through a linear fit of the measured change in volume over the droplets lifetime (i.e. $d\forall/dt$ and normalized with respect to the contact line length before depinning (see Eq. (4.1)) [57]. Thus, the evaporation rates of droplets with dissimilar contact angles are compared directly by relating the contact line length (i.e. testing the contact line dependence).

$$\dot{\pi}_{lv} = \frac{\dot{m}_{lv}}{2\pi R_0} \tag{4.1}$$

At least four experiments are conducted per setup (e.g. patterned substrate $R_P^{\text{II}} \cong 380\mu$m, $T_s = 50$℃, formed using inner fluid channel), totaling 342 data sets. This cumulative data set allows the evaluation of the error in image analysis (e.g., linear fitted evaporation rate, observed depinning time) and evaluation for the possible effects on excess flow into the droplet once the syringe pump has stopped. Figure 4.4 plots the measured evaporation rate per unit contact line length ($\dot{\pi}_{lv}$) for each substrate/temperature/droplet formation setup. As shown, $\dot{\pi}_{lv}$ follows the same trend as the substrate temperature is increased (regardless of the substrate, initial contact angle, and droplet formation method). Therefore, a single trend line can be introduced for $\dot{\pi}_{lv}(T_s)$ (independent of θ_0), contradicting Deegans model [19, 20] and reports by Dash and Garimella [16]. The largest error is observed with the non-patterned substrates implementing the channel formation (purple stars in Fig. 4.4) at high substrate temperatures. This is best explained by the error in determining the depinning time (τ_D) and the previously mentioned excess flow into the droplet causing a suppression in the evaporation rate. Overall, the averaged evaporation rate per unit contact line length ($\dot{\pi}_{lv}$) remains within the error of measurement for the entire data set.

Two conclusions are made from the results in Fig. 4.4; (1) the method of droplet formation does not affect the evaporation rate significantly enough to provide misleading results,

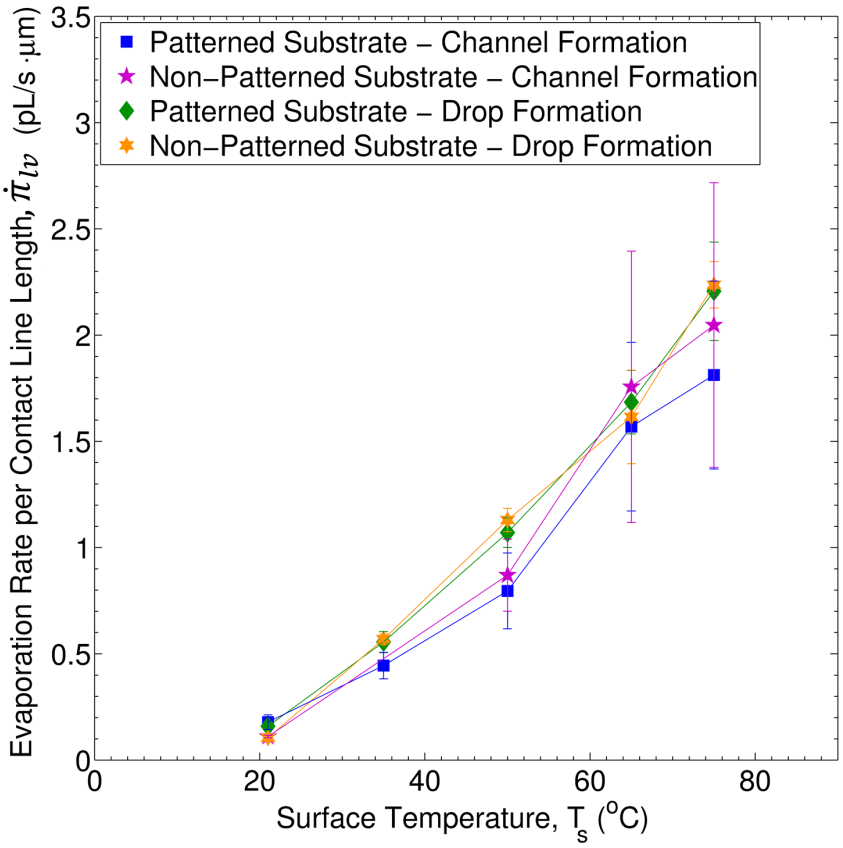

Figure 4.4: Plot of the evaporation rate per unit contact line length during an observed CCR mode of evaporation (prior to a depinned contact line, $\dot{\pi}_{lv}^{t<\tau_D}$) for various experiments on both patterned and non-patterned acrylic polymer substrates at elevated temperatures. 'Channel formation' refers to drops formed using the presented inner substrate fluid channel. 'Drop Formation' refers to droplets manually placed onto the substrate from above, using a needle/syringe. Each data point is comprised of at least four experiments.

and (2) the evaporation rate ($\dot{m}_{lv}$) has no distinct dependence on a droplets initial contact angle (for $\theta_0 \lesssim 127°$). While Dash and Garimella [16] focused on superhydrophobic surfaces ($\theta \gtrsim 160°$) which cannot be produced with the patterned substrates, the results in Fig. 4.4 contradicts the solution provided by Deegans model (see Fig. 3.3d). Regardless, with no noticeable effect on the evaporation rate, the discussed method of droplet formation (using the 'bottom-up' methodology with the inner substrate fluid channel), not only allows for steady-state microdroplet evaporation studies, but has direct implementation toward micro-cooling systems.

CHAPTER 5: NUMERICAL SIMULATIONS

5.1 Numerical Comparisons to Experimental Results

Figures 5.1 and 5.2 show comparisons between Popovs model (Eq. (3.11)) and the measured droplet volume. The experimental data is used to provide the time evolution of the contact angle for evaluating Popovs model. Numerical solutions are evaluated for both cases (1) a pinned contact line (dashed lines, termed 'Pinned Numerical Model') and (2) a depinning contact line (dotted lines, termed 'Depinned Numerical Model'). For a laser patterned substrate (Fig. 5.2), the two solutions coincide because the contact radius is constant (i.e. the contact line is pinned by the laser pattern trench). Therefore, only the pinned numerical solutions are reported for the laser patterned substrates.

Droplet evaporation on a non-patterned substrate (naturally pinned) is shown in Fig. 5.1. Comparisons of the pinned and depinned model are made for (1) a smaller droplet ($\forbidden{V}_0 \approx 100$ nL, $\theta_0 \approx 63^\circ$, see Fig. 5.1a) and (b) a larger droplet ($\forbidden{V}_0 \approx 400$ nL, $\theta_0 \approx 69^\circ$, see Fig. 5.1b). As shown in Fig. 5.1, the pinned model deviates near the end of the droplets lifetime. The subplot for the radius evolution during evaporation shows a pinned contact line is not an accurate model for the non-patterned substrates. When evaluating the pinned model, the model assumes the contact line (where a majority of the evaporation takes place, see Fig. 4.4) is larger than that observed experimentally. This result verifies our expectation of the increased role of contact line evaporation. The depinned model predicts a longer droplet lifetime and is a better representation of the evaporation on a non-patterned substrate.

Droplet evaporation on a patterned substrate $R_p \approx 475\mu$m and $R_p \approx 600\mu$m are shown in Fig. 5.2a and Fig. 5.2b respectively. The pinned numerical solutions also provide reasonable

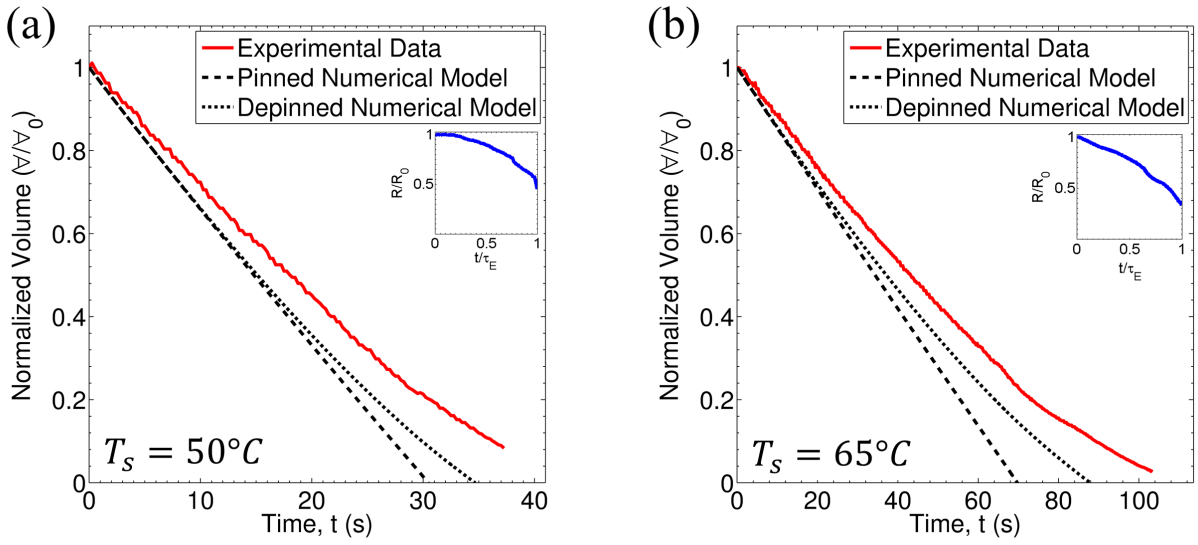

Figure 5.1: Comparison between the measured volume change (solid red lines) to the numerical solution of Eq. (3.11) for droplets on a non-patterned substrate at (a) $T_s = 50$℃ and (b) $T_s = 65$℃. Numerical solutions were evaluated by assuming a pinned contact line (dashed black line) and including the time evolution of the radius from experimental data (dotted black line). A subplot is provided of the normalized radius profile. All numerical predictions assume constant vapor surface concentration, c_s, at the substrate surface temperature. *Experimental Data*: (a) $T_s = 50$℃, $c_s = 8.3153\text{E–}8\ g/mm^3$, $R_0 \cong 460.9\ \mu$m, $\theta_0 \cong 62.9°$, $\forall_0 \cong 103.3$ nL, $h_0 \cong 278.8\ \mu$m; (b) $T_s = 65$℃, $c_s = 1.6096\text{E–}7\ g/mm^3$, $R_0 \cong 687.2\ \mu$m, $\theta_0 \cong 68.8°$, $\forall_0 \cong 402.2$ nL, $h_0 \cong 469.2\ \mu$m;

predictions for evaporation on the patterned substrates (see Fig. 5.2). Subplots of the contact radius are included for representing the accuracy in assuming a pinned contact line during evaporation. The error in the numerical model for predicting the droplets lifetime for both cases ($T_s = 50$℃ and $T_s = 65$℃) are comparable.

In all cases, the Popovs model overpredicts the evaporation rate. Because the fluid channel is located within the heated substrate, the water is preheated prior to droplet formation. Therefore, it is assumed that the initial bulk fluid temperature is equal to the substrate temperature. Once the infuse rate is terminated, it is expected that bulk temperature will decrease during evaporation [17]. This results in a temperature distribution along the liquid-vapor interface [7, 8, 16]. The numerical results in Fig. 5.1 and Fig. 5.2 are evaluated with constant surface vapor concentration (i.e. constant temperature) along the entire liquid-

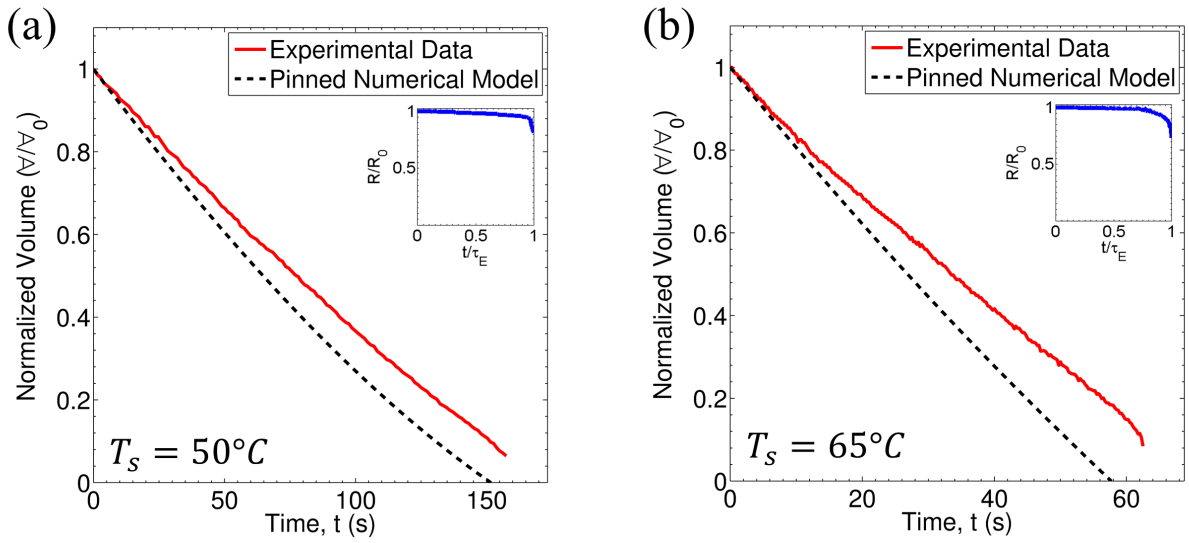

Figure 5.2: Comparison between the measured volume change (solid red lines) to the numerical solution of Eq. (3.11) for droplets on a patterned substrate of (a) $R_p \approx 475\mu$m and (b) $R_p \approx 600\mu$m. Numerical solutions were evaluated by assuming a pinned contact line. A subplot is provided of the normalized radius profile. All numerical predictions assume constant vapor surface concentration, c_s, at the substrate surface temperature. *Experimental Data*: (a) $T_s = 50$°C, $c_s = 8.3153\text{E–}8\ g/mm^3$, $R_0 \cong 469.2\ \mu$m, $\theta_0 \cong 121.0$°, $\forbidden{V}_0 \cong 583.6$ nL, $h_0 \cong 828.0\ \mu$m; (b) $T_s = 65$°C, $c_s = 1.6096\text{E–}7\ g/mm^3$, $R_0 \cong 610.0\ \mu$m, $\theta_0 \cong 77.4$°, $\forbidden{V}_0 \cong 343.9$ nL, $h_0 \cong 485.8\ \mu$m.

vapor interface. Resent publications by Briones et al. [7, 8] show that the temperature at the apex of wetted droplets is $\sim 5\%$ lower than the at the contact line. Dash and Garimella [16] show a temperature nearing 30% lower at the apex for large contact angles ($\theta \sim 160$°). This supports the consistent overprediction by Popovs model. When the surface temperature distribution is considered, the vapor concentration decreases from the contact line to the apex. The evaporation flux will therefore follow the same trend, increasing the predicted droplet lifetime. The increased degree of overprediction for the higher substrate temperatures (Fig. 5.2b) also supports this hypothesis because larger temperature gradients are expected (thus causing a larger suppression of the evaporation flux).

5.2 Correction to Numerical Model

Proposed is a correction to Deegans model and Popovs model based on the temperature distribution along the liquid-vapor interface. A temperature distribution will change the vapor concentration along the liquid-vapor interface (a boundary condition used while deriving Deegans model). This will impose a concentration gradient along the interface (i.e. variable c_s), thereby changing the evaporation flux (governed by diffusion). The modification is to change the constant surface concentration (c_s) to a variable surface concentration along the liquid-vapor interface ($c_s(\alpha, \theta)$) dependent on the temperature distribution within the droplet. Equations (5.1) and (5.2) represent the modified versions of Deegans model and Popovs model, respectively.

$$J(\alpha) = \frac{D\big(c_s(\alpha,\theta) - c_\infty\big)}{R}\left[\frac{1}{2}\sin\theta + \sqrt{2}(\cosh\alpha + \cos\theta)^{3/2} \times \int_0^\infty \frac{\cosh(\theta\tau)}{\cosh(\pi\tau)} \tanh\big[(\pi-\theta)\tau\big] P_{-1/2+i\tau}(\cosh\alpha)\tau d\tau\right] \quad (5.1)$$

$$\dot{m}_{lv} = -\pi R D\big(c_s(\alpha,\theta) - c_\infty\big)\left[\frac{\sin\theta}{1+\cos\theta} + 4\int_0^\infty \frac{1+\cosh 2\theta\tau}{\sinh 2\pi\tau}\tanh\big[(\pi-\theta)\tau\big]d\tau\right] \quad (5.2)$$

5.2.1 Temperature Distributions

Six cases are shown in Fig. 5.3 to represent the effect of (1) contact angle and (2) substrate surface temperature on the interfacial temperature distribution during droplet evaporation. The temperature gradient (contact line to apex) increases with increasing contact angle. As a result, the numerical solutions of Deegans model (Eq. (3.9)) and Popovs model (Eq. (3.11)) are less accurate for larger contact angles. Introducing a variable surface concentration along the liquid-vapor interface to Deegans model and Popovs model (Eqs. (5.1) and (5.2), respectively) will not only provide a better physical model, but they also provide higher

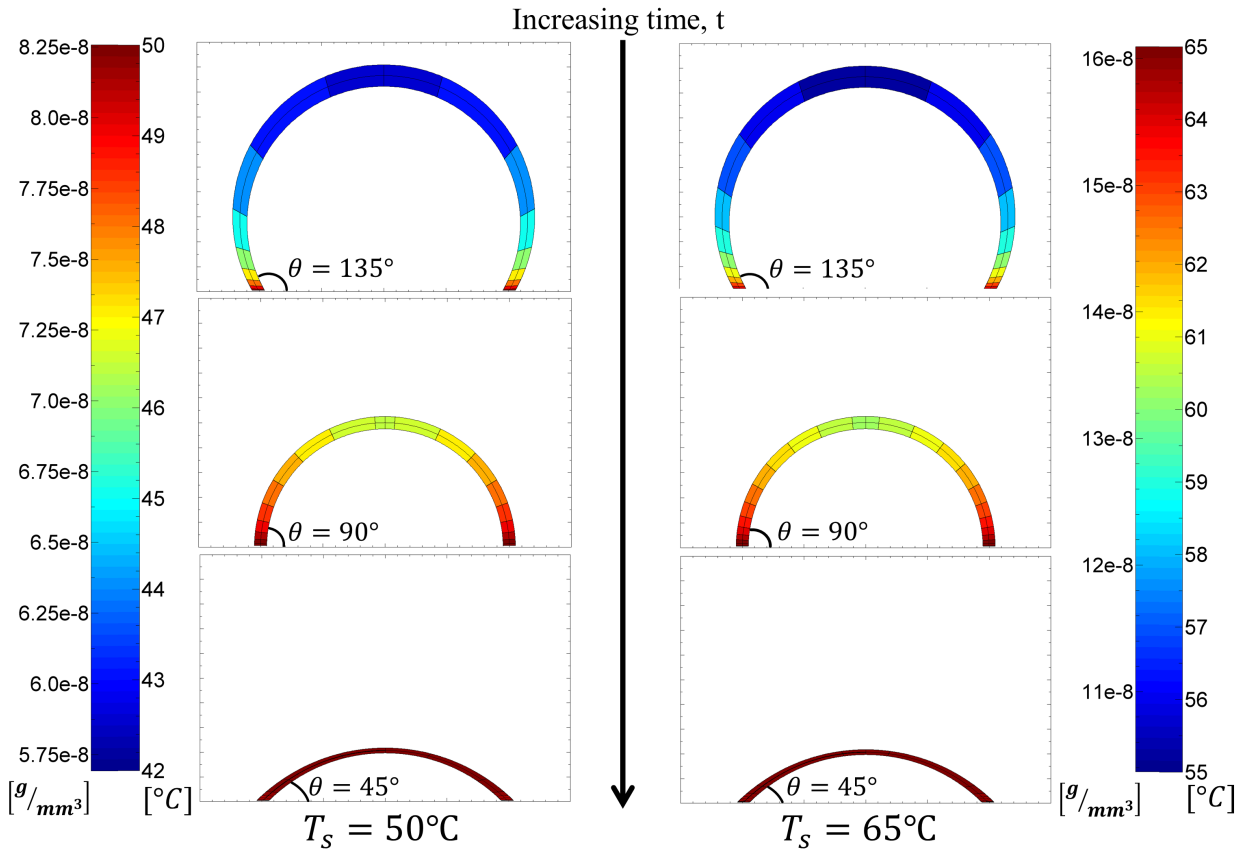

Figure 5.3: Contour plots of temperature distribution (right contour axis) and corresponding vapor concentration (left contour axis) along the liquid-vapor interface on an evaporating droplet on a heated substrate of (a) $T_s = 50℃$ and (b) $T_s = 65℃$ using the surface fit produced through interpolation of numerical results by Briones et al. [7, 8] and Dash and Garimella [16]. The thickness of the liquid-vapor interface is magnified to provide a better visual of the distribution.

accuracy when predicting droplet evaporation with large initial contact angles.

Measurements of the temperature at the liquid-vapor interface have been reported [2, 27, 43, 77], although is not practical in this study. Therefore, numerical simulations will provide a feasible method of estimating the temperature distribution as a result of the self-cooling effects during droplet evaporation. References (1) Briones et al., Fig. 8 [7] and Fig. 4 [8]; and (2) the supporting information accompanying Dash and Garimella [16] are interpolated for estimating a temperature distribution along the liquid-vapor interface. Both figures by Briones et al. [7, 8] provide isotherm contour lines at various time evolutions during

Table 5.1: Values of α and θ corresponding to an intersection between an isotherm line and liquid-vapor interface from [7, 8]. Dashed lines (–) denotes no intersection for a given isotherm line. The substrate temperature in all cases is $T_s = 373$ K (100℃)

		Fig. 8 - Reference [7]						Fig. 4 - Reference [8]			
		Droplet B		Droplet D		Droplet E		Droplet A		Droplet B	
	Temperature	α	θ	α	θ	α	θ	α	θ	α	θ
Image 1 ($t = t_1$)	360 K	–	–	–	–	–	–	0.5	78.5°	–	–
	365 K	0.3	78.5°	0	81.7°	0	83.1°	2.2	78.5°	0.4	78.5°
	370 K	2.2	78.5°	2.9	81.7°	2.6	83.1°	3.5	78.5°	2.2	78.5°
	373 K	5.0	78.5°	5.0	81.7°	5.0	83.1°	5.0	78.5°	5.0	78.5°
Image 2 ($t = t_2$)	365 K	–	–	0.1	73.3°	0.1	76.1°	1.6	70.8°	–	–
	370 K	2.1	71.6°	2.6	73.3°	3.7	76.1°	3.0	70.8°	1.9	70.8°
	373 K	5.0	71.6°	5.0	73.3°	5.0	76.1°	5.0	70.8°	5.0	70.8°
Image 3 ($t = t_3$)	370 K	–	–	2.5	36.8°	2.5	32.9°	1.6	34.0°	–	–
	373 K	5.0	34.0°	5.0	36.8°	5.0	32.9°	5.0	34.0°	5.0	34.0°

droplet evaporation. An approximate value of α (representing a point along the liquid-vapor interface) is found at the intersection of the liquid-vapor interface and each isotherm line. Each intersection point of α and T_{iso} (the isotherm temperature) are documented with the calculated contact angle (based on the apex height and contact radius using Eq. (5.3)).

$$\theta = \frac{\pi}{2} - \sin^{-1}\left(\frac{R-h}{R}\right) \tag{5.3}$$

Table 5.1 provides a summary of the values for α, θ, and corresponding isotherm (interface) temperature.

Dash and Garimella [16] provided temperature contours within a droplet evaporating at room temperature ($T_s = 21$℃) on hydrophobic ($\theta = 110°$) and a superhydrophobic ($\theta = 160°$) substrates. The α values intersecting the liquid-vapor interface at the center of the contour

Table 5.2: Interpreted temperature values and the corresponding α value along the liquid-vapor interface from the plots provided by the supporting information from [16]. Substrate temperature is at $T_s = 20.5$℃

	T (℃)	α
$\theta = 110^\circ$	18.2	0
	18.3	0.2
	18.4	0.5
	18.5	0.6
	18.8	1.1
	19.4	1.6
	19.7	2.4
	20.5	5.0
$\theta = 160^\circ$	13.9	0
	14.0	0.05
	14.1	0.1
	14.2	0.2
	14.5	0.3
	14.8	0.45
	15.2	0.55
	15.5	0.65
	16.8	1.0
	18.3	1.5
	20.5	5.0

lines are documented for finding the temperature distribution along the liquid-vapor interface for each provided contact angle, similar to the previous discussion. A summary of the documented values are shown in Table 5.2.

Three separate matrices are generated from the compiled data in Tables 5.1 and 5.2, and a surface fit is performed for each matrix to provide $T_{fit} = T(\alpha, \theta)$, where T_{fit} is a surface

fitted solution. The three surface fits include (1) using the data collected from the solutions provided by Briones et al. [7, 8] (Table 5.1); (2) using the data collected from the solutions provided by Dash and Garimella [16] (Table 5.2); and (3) combining the interpolations found for each reference for a cumulative data set. All isotherm temperature values are normalized with respect to the substrate surface temperature (i.e. $T_{fit} = T_{iso}(\alpha, \theta)/T_s$). Separate interpolation matrices are generated for comparing the increase in prediction from the data collected from each reference, thus evaluating the accuracy of each numerical simulation.

A lowess smoothing fit is implemented to correlate $T_{iso}(\alpha, \theta)$ and T_s with the data gathered in Table 5.1 and 5.2, where T_{iso} is the temperature corresponding to the isotherm lines intersecting the liquid-vapor interface (i.e. various temperatures along the interface) and T_s is the substrate surface temperature. This fitted temperature distribution (T_{fit}) provides a temperature along the interface (α) for a given contact angle (θ). This relation is used to predict a temperature distribution for experimental data at each elevated substrate temperature. For relating the evaporation rate to the temperature distribution, the vapor concentration distribution along the interface is needed. By the Clausius-Clapeyron equation (Eq. (1.4)), the temperature is directly related to the vapor concentration. All experiments performed remain within $T \in [20, 100]$ ℃ (e.g. not cooling below room temperature nor approaching nucleate boiling (see Fig. 1.2)). For simplicity, a polynomial curve is generated within this temperature range that relates temperature to the vapor concentration. While this polynomial curve may not be well representative over the entire liquid water regime, it provides a sufficient fit over the experimental range (21℃ – 75℃) A plot of known vapor concentrations at various temperatures [12] along with the fitted polynomial curve is shown in Fig. 5.4.

With the resulting temperature surface fit $T_{fit} = T(\alpha, \theta)$ interpolated from the listed references [7, 8, 16], and polynomial fit of vapor concentration $c = c(T)$ (or $c_s = c_s(T)$ when considering the droplets surface vapor concentration, Fig. 5.4), the vapor concentration

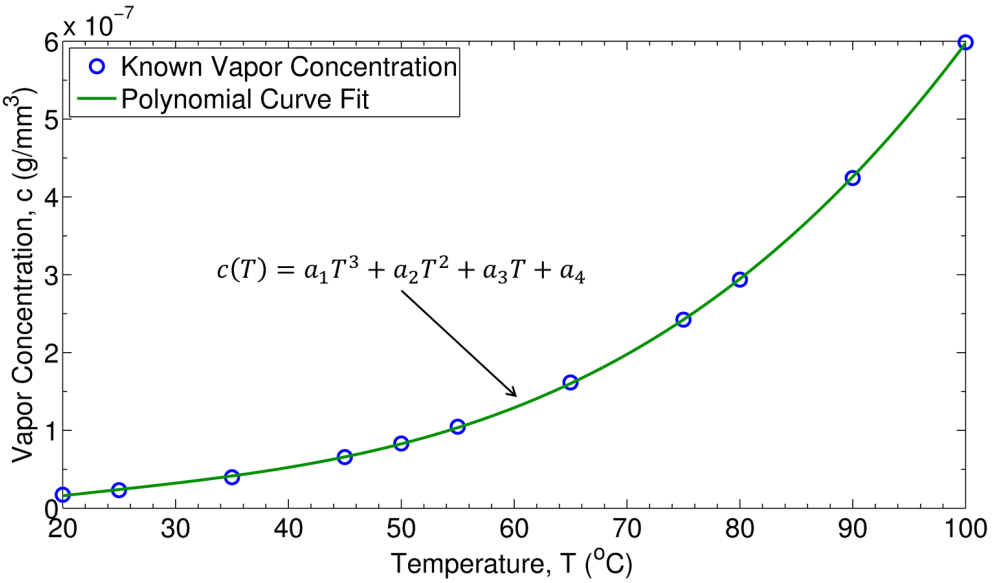

Figure 5.4: A plot providing various known vapor concentrations (blue circles) within the temperature range of the conducted experiments. The data points are fit to a third order polynomial (green line).

along a droplets entire liquid-vapor interface can be found based on the substrate surface temperature. These corresponding distributions of temperature and surface concentration during droplet evaporation on heated substrates of $T_s = 50$℃ and $T_s = 65$℃ are provided in Fig. 5.3, previously shown.

5.2.2 Modified Model Improvements

The fitted temperature distribution provides a variable surface concentration along the liquid-vapor interface. Evaluation of the modified numerical models (Eqs. (5.1) and (5.2)) are presented in the following sections. A numerical comparison between Deegans model is discussed, as well as experimental comparisons to Popovs model for (1) validating the improvements of the presented modifications and (2) determining any dominating effects of a droplets self-cooling induced temperature distributions.

Deegans Model for Evaporation Flux

To demonstrate the difference between the two models of the local evaporation flux (Deegans model with constant surface concentration and the modified model with variable surface concentration), the solution of the evaporation flux for both models are compared at various contact angles (see Fig. 5.5). The dashed lines represent the evaporation flux solution evaluated using Deegans model (Eq. (3.9)), and the solid lines are the solution of the modified model (Eq. (5.1)). To maintain clarity, the solutions of the dotted lines in Fig. 5.5 (Deegans model, assuming constant c_s) are identical to the solutions in Figs. 3.2 and 3.3. Additionally, Figs. 5.6 and 5.7 exploit the difference between the two numerical solutions for each contact angle with a representative vector plot of the evaporation flux (J) along the interface.

The temperature distribution induced from the self-cooling effects ('evaporative cooling') during evaporation significantly alters the evaporation flux. The increased thermal resistance for larger droplets (larger contact angles) creates larger temperature gradients (contact line to apex, Fig. 5.3). Figure 5.5 best represents the increase in deviation between the two models due to this increase in thermal resistance. An implicit boundary condition for the temperature distribution along the interface (based on the numerical solutions interpreted [7, 8, 16]) is the temperature at the contact line is equal to the substrate surface temperature ($T_{fit}^{\alpha\to\infty} = T_s$), whereas Deegans model assumes the temperature across the entire interface is at the substrate surface temperature. As shown, the results of both models converge to the same magnitude of evaporation flux as $r \to R$ (the contact line). Thus, the solution of the modified model agrees with the implicit boundary condition.

A major improvement with the modified model is based on the change of curvature of the solution from the apex ($\alpha = 0, r/R = 0$) to the contact line ($\alpha \to \infty, r/R = 1$) for contact angles $\theta \geq 90°$(solid red, pink, and green lines in Fig. 5.5). The solution of Deegans

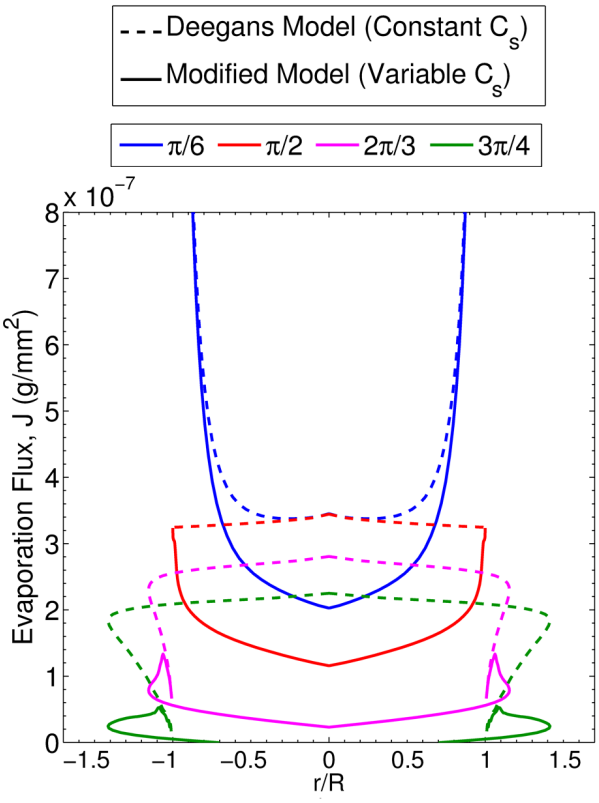

Figure 5.5: Comparison of evaporation flux solutions calculated from the numerical model assuming constant vapor concentration (dashed lines) and the modified model with variable vapor concentration (solid lines). *Numerical Data:* See Fig. 3.2. Solutions with variable c_s distribution are evaluated from $T_{fit}(\alpha, \theta)$ with a substrate surface temperature of $T_s = 20$℃.

model shows the largest evaporation flux for hydrophobic droplets ($\theta > 90°$) is at the apex, and suppresses near the contact line. This disagrees with the data presented in Section 4.2 (Fig. 4.4) and the results/conclusions provided by many authors on contact line dependence on evaporation rate [1, 5, 7–9, 13, 15, 17, 46, 48, 52, 57, 58, 61, 65, 69, 75]. The modified model maintains a high evaporation flux near the contact line and a minimum at the apex regardless of contact angle, hence a contact line dependence. Thus, the modified model provides theoretical solutions (Figs. 5.6 and 5.7) of droplet evaporation in good agreement with previous publications [1, 5, 7–9, 13, 15, 17, 46, 48, 52, 57, 58, 61, 65, 69, 75] and the data presented in Section 4.2 (Fig. 4.4).

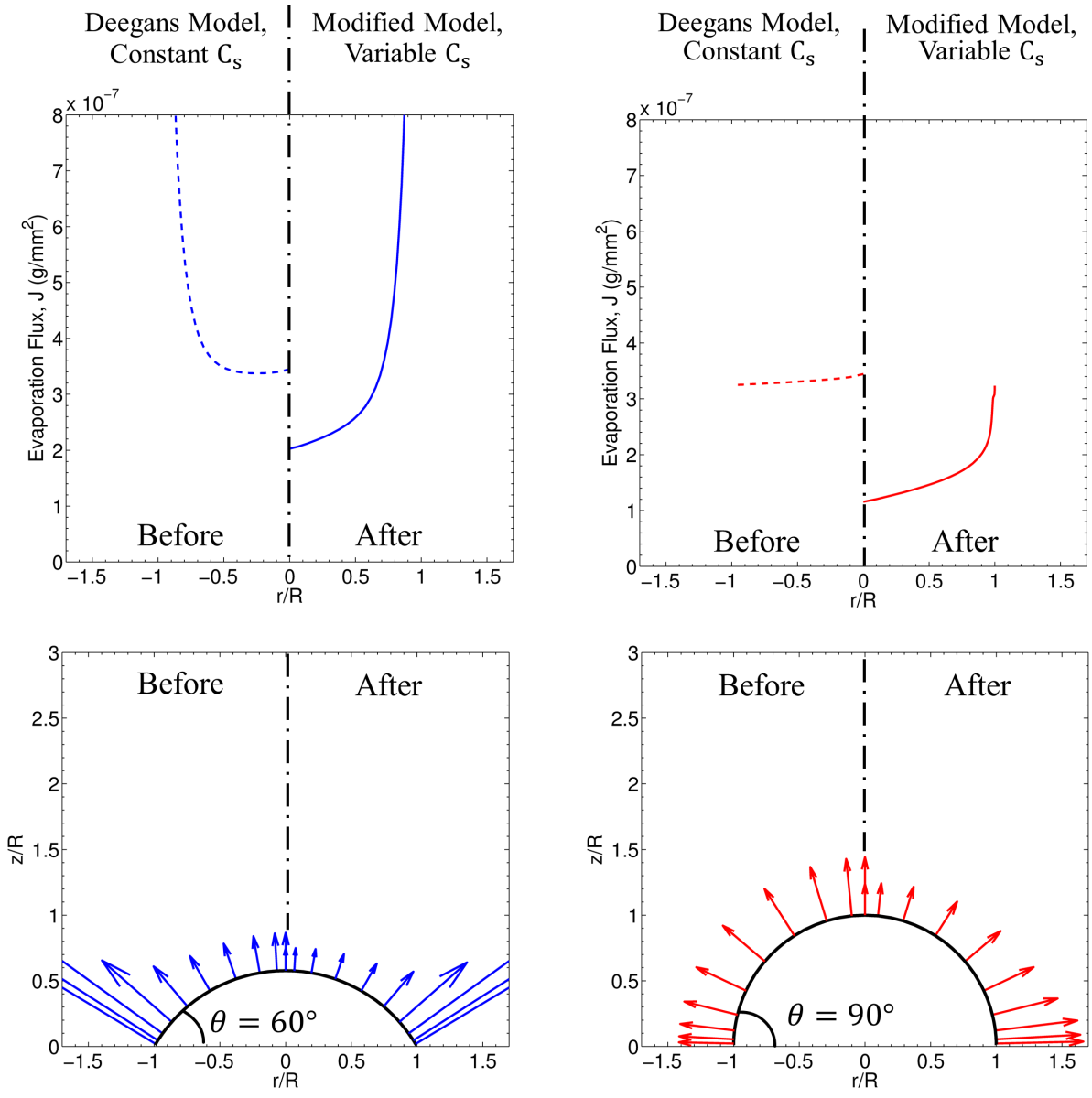

Figure 5.6: Magnitude and vector plot comparisons of the evaporation flux, J, of (left) Deegans model before modifications and (right) the modified model (i.e. c_s distribution) for wetted droplets. The top figures are partially represented in Fig. 5.5

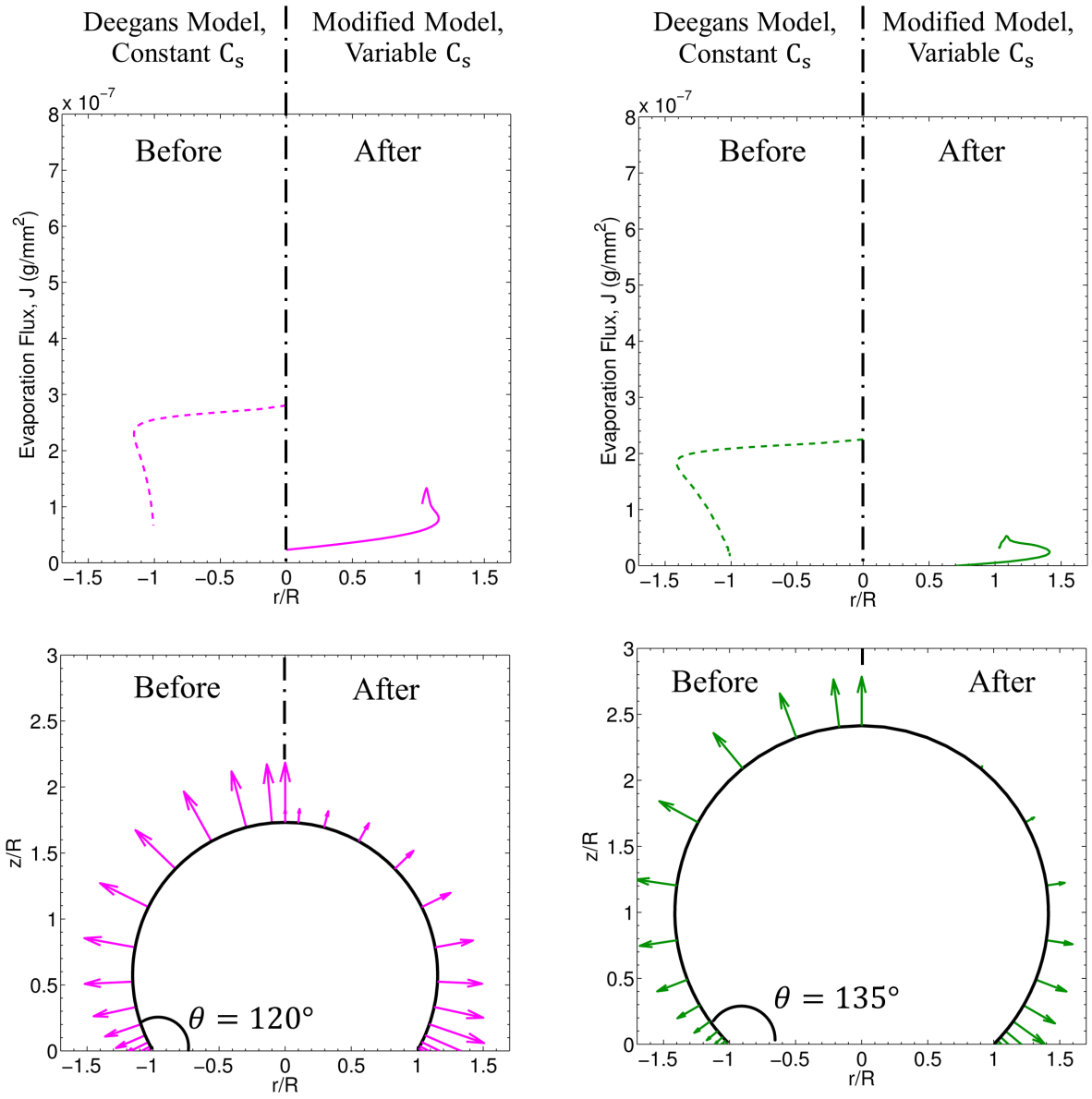

Figure 5.7: Magnitude and vector plot comparisons of the evaporation flux, J, of (left) Deegans model before modifications and (right) the modified model (i.e. c_s distribution) for hydrophobic droplets. The top figures are partially represented in Fig. 5.5

Popovs Model for Evaporation Rate

To further evaluate the corrected model, Popovs model (derived from Deegans model) is compared to experimental data. The numerical solution assuming constant vapor concentration (Eq. (3.11)) and the proposed modification of surface vapor concentration (Eq. (5.2)) are compared to experimental data in Fig. 5.8. Because the temperature gradient is decreasing from the contact line to the apex, the evaporation rate is expected to be lower in comparison to the numerical models that assumed a constant vapor concentration – Eqs. (3.9) and (3.11). This hypothesis has been confirmed theoretically from the previous analysis on evaluating the improvements of Deegans model (Figs. 5.5, 5.6, and 5.7). The vapor surface/interface concentration distribution, $c_s(\alpha, \theta)$, is introduced from the data gathered in Fig. 5.3 and Tables 5.1 (termed 'Briones et al. interpolated model') and 5.2 ('Dash and Garimella interpolated model'). A combined model includes a superposition of Briones et al. and Dash and Garimella interpolated matrix models.

Comparisons of the predicted evaporation rate are shown for both $T_s = 50$℃ (Fig. 5.8a) and $T_s = 65$℃ (Fig. 5.8b). All the models for both heated substrates ($T_s = 50$℃ and $T_s = 65$℃) show very similar error accumulation over the droplets lifetime. The modified models provide a higher accuracy in estimating the droplets lifetime. The combined model provides the most accurate model, presumable to the range of contact angles, substrate temperatures, and largest number of interpolated data points. Table 5.3 provides the error analysis for all four models.

All three models showed an increase is accuracy when predicting the droplets lifetime. The Briones et al.[7, 8] model shows the least improvement. This can be explained by (1) lack of known temperature points along the interface to provide a sufficient temperature distribution and (2) the numerical results are for a substrate surface temperature of $T_s =$ 100℃ (much larger than experimental data). This can lead to false temperature gradients

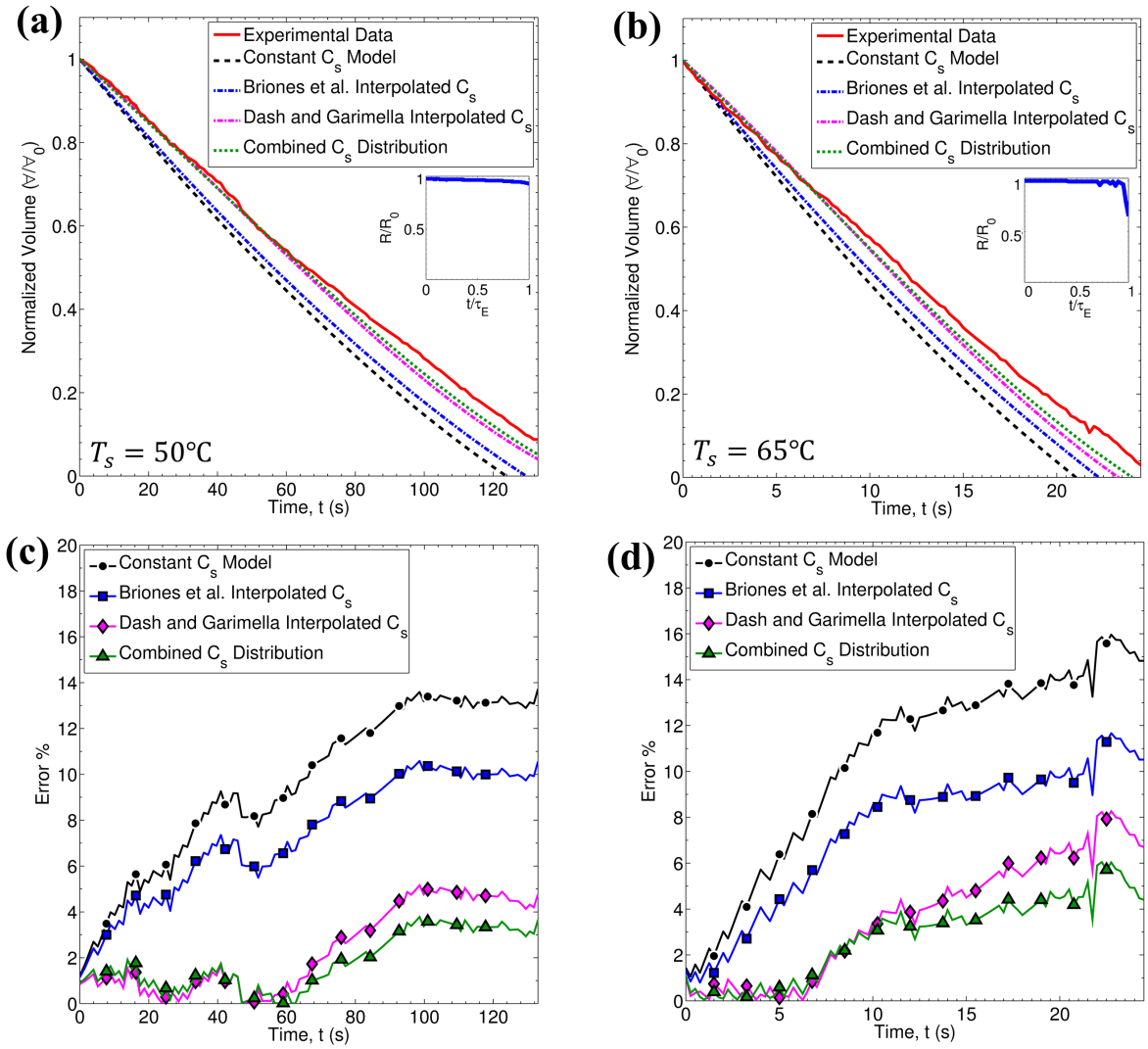

Figure 5.8: Plots comparing experimental data (solid red lines), numerical solutions obtained from Eq. (3.11) assuming constant temperature along interface (dashed black lines), and the solution from the proposed modification in Eq. (5.2) with variable vapor surface concentration (dot-dashed lines). Experiments were performed on patterned substrate at (a) $T_s = 50$℃ and (b) $T_s = 65$℃. The relative errors are shown in (c) and (d) *Experimental Data*: (a) $R_0 \cong 455.4\ \mu$m, $\theta_0 \cong 117.4^{\circ}$, $\forbidden{V}_0 \cong 459.4$ nL, $h_0 \cong 745.2\ \mu$m, $\tau_E \cong 133.0\ s$; (b) $R_0 \cong 394.7\ \mu$m, $\theta_0 \cong 106.6^{\circ}$, $\forbidden{V}_0 \cong 205.7$ nL, $h_0 \cong 527.2\ \mu$m, $\tau_E \cong 24.5\ s$

Table 5.3: Error for each of the four models analyzed for predicting the droplets lifetime. The linearized error is the error in slope of the linear fitted curve of each curve provided in Fig. 5.8.

	Linearized error		Max error	
Interpolated Model	$T_s = 50$℃	$T_s = 65$℃	$T_s = 50$℃	$T_s = 65$℃
Popovs model (Constant c_s)	9.70%	10.54%	13.72%	15.97%
Briones et al. [7, 8]	7.44%	7.43%	10.58%	11.67%
Dash and Garimella [16]	2.40%	3.69%	5.16%	8.27%
Superimposed/Combined model	1.84%	2.83%	3.78%	6.05%

along the liquid-vapor interface due to the substrate temperature of the experimental data being considerably lower. The interpolation gathered from the results provided by Dash and Garimella [16] provided higher accuracy. A larger data set for the temperature distribution is gathered, which provides a better surface fit. Although, inaccurate predictions still exist due temperature distribution may be due to the lack of data with respect to the contact angle evolution during evaporation (assuming a pinned contact line). The interpolation is expected to decrease in accuracy for smaller contact angles ($\theta < 110°$). The combined model shows the greatest prediction for both substrate temperatures. The interpolation from Briones et al. [7, 8] provides sufficient data for contact angle evolutions during evaporation as well as for temperature distribution for low contact angles, while the Dash and Garimella [16] interpolation provides a better temperature distribution along the interface and increases the range of contact angles.

This combined model for estimating the surface vapor concentration increases the accuracy in predicting the droplets lifetime by $\sim 10\%$. Compared to Popovs model (with a constant surface concentration), the combined interpolated model increased the accuracy in predicting the droplets lifetime by $\sim 7.7\%$ and $\sim 9.9\%$ for $T_s = 50$℃ and $T_s = 65$℃, respectively. As a result, the predicted droplet evaporation remains within 2% – 4% of the experimentally measured evaporation rate.

CHAPTER 6: CONCLUSIONS

Experimental and numerical investigations of water microdroplet evaporation are presented. A laser patterned substrate is fabricated for controlling the dynamics of the contact line during droplet evaporation, where a moat-like trench pins the contact line and forces the droplet to undergo a time-extended constant contact radius (CCR) mode of evaporation. This methodology also facilitates (1) precise control of droplet formation, size, and wetting dynamics, (2) droplet heating prior to formation, and (3) future steady-state evaporation studies on heated surfaces with a variety of different non-equilibrium contact angles (including $\theta > \theta_a$) for a given solid-liquid-vapor system (e.g., steady-state studies of both wetted and non-wetted droplets on a single substrate).

Numerical solutions provided by Deegan et al. [19, 20] and Popov [54] are used for comparisons to experimental data, which consistently overpredicts the droplets lifetime. The implementation of constant vapor concentration in both models is assumed to be a key source of error because the droplets surface/interface temperature is not constant (i.e., the apex temperature of the droplet should be less than the substrate temperature during evaporation [7, 8, 16, 38, 69]). In result, both Deegans model and Popovs model are modified by considering the temperature distribution along the liquid-vapor interface (interpolated using results reported by Briones et al. [7, 8] and Dash and Garimella [16]). Evaluation of Deegans modified model results in a model that better represents a widely accepted concept of contact line dependence on droplet evaporation. In comparison to Popovs model, the modified Popov model shows an increase in droplet lifetime and yields a better prediction of τ_E in comparison to experimental data. This combined model for estimating the surface vapor concentration increases the accuracy in predicting the droplets lifetime by $\sim$ 10%.

Compared to Popovs model (with a constant surface concentration), the combined interpolated model increased the accuracy in predicting the droplets lifetime by $\sim 7.7\%$ and $\sim 9.9\%$ for $T_s = 50$℃ and $T_s = 65$℃, respectively. As a result, the predicted droplet evaporation remains within 2% – 4% of the experimentally measured evaporation rate. The reduced error in predicting the droplets lifetime provides encouragement toward understanding the dynamics of microdroplet evaporation.

APPENDIX A: MATLAB CODE FOR EVALUATING DEEGANS MODEL

```
%Evaluation of evaporation flux
clc
clear all

%% Input Plot type
y_n = 0;
        %0 - Evap Flux plot
        %1 - vector plot

%% Input Method of solution
cs_yn = 1;
        %0 - Constant surface concentration
        %1 - Variable surface concentration
    T = 20;%C - Substrate temperature of simulation

    double = 1; %type of plot
        %0 - plot 0 to R
        %1 - plot -R to R

%% Input Contact Angle
% theta_imp = degtorad(135);
% theta_imp = 3*pi/4;
theta_imp = [pi/3, pi/2, 2*pi/3, 3*pi/4];


%% Input Experimental Conditions
R = 0.6; %mm
D = 26.1; %mm^2/s
c_inf = 7.34116E-9; %g/mm^3  40% humidity, T = 20C

%Calling vapor concentration surface fit
if cs_yn == 0 %constant
    c_s = Temp_to_Cs_Func(T,[]); %g/mm^3
elseif cs_yn == 1 %variable
    theta_save = theta_imp;%avoiding overwrite
    run('Briones_Data')
        alpha_B = alpha; %avoid overwriting alpha
        theta_B = theta; %avoid overwriting theta
    run('Dash_Data')
        alpha = [alpha_B, alpha]; %compiling both data sets
        theta = [theta_B, theta]; %compiling both data sets
        Temp_Dist = [Normed_Temp_Briones, Normed_Temp_Dash];
```

```
43      cs_func = Temp_to_Cs_Func(T*Temp_Dist);
44      cs_fit = fit([alpha', theta'], cs_func, 'lowess', ...
45          'Span', .50, 'Robust', 'Bisquare');
46          clear ('alpha')
47          clear('theta')
48          theta_imp = theta_save;
49  end
50
51  %% Numerical code
52  %defining 'tau' [t] limits and step size
53  for ii = 1:length(theta_imp)
54      theta = theta_imp(ii);
55
56  t_del = 1e-2;
57  t_max = 10;
58  t_iter = t_max/t_del;
59
60  %defining 'xi' [x] limits and step size
61  %   (legendre function integration)
62  x_del = 1e-2;
63  x_max = 10;
64  x_iter = x_max/x_del;
65
66  %defining limit and step size of alpha [a]
67  a_max = 5;
68  if y_n == 0 %Flux evaluation
69      a_del = 1e-1;
70      a_iter = a_max/a_del;
71  else %vector plot evaluation
72      a_del = 1e-1;
73      if theta > pi/2
74          a_del = a_del/2;
75      end
76      a_iter = (1 + sqrt(8*(a_max)/(a_del)))/(2);
77  end
78
79  %begin evaluation
80  for k = 1:a_iter %along droplet liquid-vapor interface
81      %analysis type for plot generation
82      if y_n == 0
83          a = (k-1) * a_del; %evap flux
84      else
```

```
85          a = (k * (k-1))/2 * a_del; %vector
86      end
87
88      %avoid singularities
89      if a == 0
90          a = 10^-4;
91      end
92
93      %Constant vs. Variable surface concentration initiation
94      if cs_yn == 1;
95          c_s = cs_fit(a, theta);
96      end
97
98  for i = 1:t_iter %tau integration
99         t1 = (i-1)*t_del;
100        t2 = (i)*t_del;
101
102     if t1 ~= 0;
103             for j = 1:x_iter  %Legendre integration
104             x1 = (j-1)*x_del;
105             x2 = (j)*x_del;
106
107             if x1 > a
108                 Pn_1(j) = (x_del)/2 * ((sin(t1 * x2) / ...
109                     sqrt(2*cosh(x2) - 2*cosh(a))) +  ...
110                     (sin(t1 * x1) / sqrt(2*cosh(x1) - ...
111                     2*cosh(a))));
112                 Pn_2(j) = (x_del)/2 * ((sin(t2 * x2) / ...
113                     sqrt(2*cosh(x2) - 2*cosh(a))) +  ...
114                     ((sin(t2 * x1) / sqrt(2*cosh(x1) - ...
115                     2*cosh(a)))));
116             else
117                 Pn_1(j) = 0;
118                 Pn_2(j) = 0;
119             end
120         end
121
122     %Sum of all sections for integral evaluation of
123     %Legendre Function
124     Int_Pn_1 = sum(Pn_1);
125     Int_Pn_2 = sum(Pn_2);
126
```

```
127         %Integral within J(r)
128             %hydrophilic
129             if theta < pi/2 && t1 > a
130                 E(i) = t_del/2 * (((cosh(theta*t1) / ...
131                     cosh(pi*t1)) * tanh((pi - theta)*t1) * ...
132                     t1 * (2/pi * coth(pi*t1) * Int_Pn_1)) + ...
133                     ((cosh(theta*t2) / cosh(pi*t2)) * ...
134                     tanh((pi - theta)*t2) * t2 * ...
135                     (2/pi * coth(pi*t2) * ...
136                     Int_Pn_2)));
137 
138             %hydrophobic
139             else
140                 E(i) = t_del/2 * (((cosh(theta*t1) / ...
141                     cosh(pi*t1)) * tanh((pi - theta)*t1) * ...
142                     t1 * (2/pi * coth(pi*t1) * Int_Pn_1)) + ...
143                     ((cosh(theta*t2) / cosh(pi*t2)) * ...
144                     tanh((pi - theta)*t2) * t2 * ...
145                     (2/pi * coth(pi*t2) * Int_Pn_2)));
146             end
147         end
148     end
149 
150     %Sum of all sections for integral evaluation
151     Int_E = sum(E);
152 
153     %Final evaluation of local evaporation flux
154     J_Flux(ii,k) = (D*(c_s - c_inf))/ R * (sin(theta) / 2 + ...
155                 sqrt(2) * (cosh(a) + cos(theta))^(3/2) * ...
156                 Int_E);
157 
158     %Tracking progress of solution
159     fprintf('%s %g %s %g %s %g %s %g \n', ...
160         'Local Iteration', k, '/', floor(a_iter), ...
161         'of Global Iteration', ii, '/', length(theta_imp))
162     end
163 
164     %% Plotting Evaporation Flux
165     if y_n == 0
166         k = 1:a_iter;
167         a = (k-1) * a_del;
168         r_plot = sinh(a)./(cosh(a) - cos(pi - theta));
```

```
169      z_plot = sin(pi-theta)./(cosh(a) - cos(pi - theta));
170
171  %Plot solution of evap flux
172      figure(1)
173      hold all
174      set(gca,'FontSize',20)
175      plot(r_plot,J_Flux(ii,:));figure(gcf)
176      plot(-r_plot,J_Flux(ii,:));figure(gcf)
177      if double == 0
178          axis([0, 1.7, 0, 15e-7])
179      elseif double == 1
180          axis([-1.7, 1.7, 0, 15e-7])
181      else
182          disp('Error in double plot - Line 16')
183      end
184      axis square
185      box on
186      xlabel('r/R')
187      ylabel('Evaporation Flux, J (g/mm^2)')
188      set(gca,'XMinorTick','on')
189      set(gca,'YMinorTick','on')
190  else
191  %% Vector Flux Plot
192      for k = 1:a_iter;
193          a(k) = (k * (k-1))/2 * a_del;
194      end
195
196      %r/R and z/R plot values
197      r_plot = sinh(a)./(cosh(a) - cos(pi - theta));
198      z_plot = sin(pi-theta)./(cosh(a) - cos(pi - theta));
199
200      b2 = pi-theta;
201      a2 = -a_max:a_del:a_max;
202          for j = 1:length(a2);
203              r_vec(j,:) = sinh(a2(j)) ./ (cosh(a2(j)) - cos(b2));
204              z_vec(j,:) = sin(b2) ./ (cosh(a2(j)) - cos(b2));
205          end
206
207      %calculating normal to surface for vector plot
208      r_norm = 2*(r_plot)./ ...
209          sqrt((2*r_plot).^2+(2*(z_plot - cot(pi-theta))).^2 + 1);
210      z_norm = 2*(z_plot - cot(pi-theta))./ ...
```

```
211         sqrt((2*r_plot).^2+(2*(z_plot - cot(pi-theta))).^2 + 1);
212
213     figure(2)
214     hold all
215     set(gca,'FontSize',20)
216     set(gca,'XMinorTick','on')
217     set(gca,'YMinorTick','on')
218
219     plot(r_vec,z_vec,'red',...
220             'LineWidth',2);figure(gcf)
221         axis equal
222         box on
223         xlabel('r/R')
224         ylabel('z/R')
225         axis([-1.7, 1.7, 0, 3])
226
227         %Vector plot, with modified scaling.
228     if theta < pi/2 %hydrophilic
229         quiver(r_plot,z_plot,J_Flux.*r_norm,J_Flux.*z_norm,...
230             25,'blue','LineWidth',2);
231         quiver(-r_plot,z_plot,-J_Flux.*r_norm,J_Flux.*z_norm,...
232             25,'blue','LineWidth',2);
233         figure(gcf)
234     elseif theta == pi/2 %uniform flux
235         quiver(r_plot,z_plot,J_Flux.*r_norm,J_Flux.*z_norm,...
236             0.5,'blue','LineWidth',2);
237         quiver(-r_plot,z_plot,-J_Flux.*r_norm,J_Flux.*z_norm,...
238             0.5,'blue','LineWidth',2);
239         figure(gcf)
240     else %hydrophobic
241         quiver(r_plot,z_plot,J_Flux.*r_norm,J_Flux.*z_norm,...
242             0.3,'blue','LineWidth',2);
243         quiver(-r_plot,z_plot,-J_Flux.*r_norm,J_Flux.*z_norm,...
244             0.3,'blue','LineWidth',2);
245         figure(gcf)
246     end
247 end
248
249 end
```

APPENDIX B: MATLAB CODE FOR EVALUATING POPOVS MODEL

```
%%Calculate dM/dt from the integral transformed Laplace solution
clear all
clc
close all

%% Variable C_s
yn_cs = 0;
        %0 - Superimposed plot of all results
        %1 - Constant surface concentation
        %2 - Briones Interpolation of temperature distribution
        %3 - Dash        '          '           '           '
        %4 - Briones and Dash       '           '           '

%% Plot Types
plot_type = 1;
        %1 - Normalized Volume
        %2 - Normalized Volume and Time

 %pinned or unpinned predictions
 yn_pin = 1;
        %1 - Pinned
        %2 - Unpinned -> R(t)

%% Error Analysis
er = 2;
    %1 - No error analysis
    %2 - Error analysis

%% Oct26 Data Input
load(fullfile('Data','Oct26DataSet', ...
    '50C','RoomDrop','Test1.dat'));
        %50C, 65C
        %380um, 600um, RoomDrop, HeatDrop, MP
    %(folder1,folder2,...,file) raw data import
Test_Data = Test1; %Renaming data for general use
Ts = 50; %C

%% Jan3 Data Input
% load(fullfile('Data','Jan3DataSet', ...
%     'Channel','600um','35C','Test1.dat'));
%         %21C, 35C, 50C, 65C, 75C
%         %250um, 380um, 600um, Channel, Old450
```

```
%     %(folder1,folder2,...,file) raw data import
% Test_Data = Test1; %Renaming data for general use
% Ts = 35; %C

%% Data Formating
if yn_cs == 0;
    iter = 4;
else
    iter = 1;
end

for k = 1:iter %Performing all methods
    if iter == 4
        yn_cs = k;

        if k ~= 1 %clearing files to avoid superimposed sol.
            clear('M_int')
            clear('M')
            clear('dV')
            yn_cs = k;
        end
    else
        %keep yn_cs the same
    end


%% Vector Inputs for Variable Surface Concentration
    %
    %
    %A. M. Briones, J. S. Ervin, L. W. Byrd, S. A. Putnam,
    %A. White, and J. G. Jones. Evaporation Characteristics
    %of Pinned Water Microdroplets. Journal of Thermophysics
    %and Heat Transfer, 26:480-493, 2012.
    %
    %
    %A. Briones, J. Ervin, L. Byrd, S. Putnam, J. Jones,
    %and A. White. Effect of Accommodation Coeffcient, Curvature
    %and Three-Dimensional Flow on the Evaporation
    %Characteristics of Pinned Water Microdroplets. 42nd AIAA
    %Thermophysics Conference,July 2011.
    %
    %
```

```
85      %S. Dash and S. V. Garimella. Droplet Evaporation Dynamics
86      %on a Superhydrophobic Surface with Negligible Hysteresis.
87      %Langmuir, 29(34):10785-10795, 2013.
88
89      if yn_cs == 1;
90          c_s = Temp_to_Cs_Func(Ts); %Cs(T) polyfit
91      else
92          if yn_cs == 2
93              run('Briones_Data')
94                  Temp_Dist = NormT_Briones;
95                  %alpha called
96                  %theta called
97
98          elseif yn_cs == 3
99               run('Dash_Data')
100                 Temp_Dist = NormT_Dash;
101                 %alpha called
102                 %theta called
103
104         elseif yn_cs == 4
105             run('Briones_Data')
106                 alpha_B = alpha; %avoid overwriting alpha
107                 theta_B = theta; %avoid overwriting theta
108             run('Dash_Data')
109                 alpha = [alpha_B, alpha]; %compiling data sets
110                 theta = [theta_B, theta]; %compiling data sets
111                 Temp_Dist = [NormT_Briones, NormT_Dash];
112
113         else
114             disp('Reason for error:')
115             disp('Invalid yn_cs Value')
116         end
117
118     %Finding vapor concentration distribution
119     c_s = Temp_to_Cs_Func(Ts*Temp_Dist);
120         if yn_cs == 3 %cannot fit 2nd order with 2 theta values
121             cs_fit = fit([alpha', theta'], c_s, 'poly21');
122         else
123             cs_fit = fit([alpha', theta'], c_s, 'poly22');
124         end
125     end
126
```

```
%% Data Calling
%These are called from the raw data input variables
%'Experiement Specific' Conditions
R_dat = Test_Data(:,3)*10^(-3); %mm
Test_Data(:,1) = Test_Data(:,1) - Test_Data(1,1); %start at t=0
Vi = Test_Data(1,5); %nL or ug
time_step = mean(diff(Test_Data(:,1))); %sec
theta_dat = Test_Data(:,4);

%Defining the number of theta interations (length of data vector)
tq_max = length(theta_dat);

%Other parameters
D = 26.1; %mm^2/s
c_inf = 0.4*Temp_to_Cs_Func(20); %40% humidity

%%%%%  Integration Parameters  %%%%%
%defining 'tau' [t] limits and step size
t_del = 1e-2;
t_max = 10;
t_iter = t_max/t_del;

%defining 'xi' [x] limits and step size
%   (legendre function integration)
x_del = 1e-2;
x_max = 10;
x_iter = x_max/x_del;

%defining limit and step size of alpha [a]
alpha_vec = 10^-3:5/(length(theta_dat)):5;

%%  Begin Evaluation  %%%%%
for tq = 1:tq_max; %contact angle
        theta = degtorad(theta_dat(tq)); %converting to radians
        if yn_pin == 1; %Pinned
            R = mean(R_dat(1:5));
        elseif yn_pin == 2; %R(t)
            R = R_dat(tq);
        else
            disp('Reason for error:')
            disp('Invalid yn_pin Value')
        end
```

```
169         time(tq) = (tq-1) * time_step;
170         alpha = alpha_vec(tq);
171 
172      if yn_cs ~= 1;
173          c_s = cs_fit(alpha,theta);
174      end
175 
176 %calculating dM/dt
177     for ii = 1:t_iter
178         t1 = (ii-1)*t_del;
179         t2 = (ii)*t_del;
180             if t1 == 0 %singularity at 1/sinh(0)
181                 t1 = 10^-4;
182             end
183         M_int(ii) = t_del/2 * ((((1 + cosh(2*theta*t1)) / ...
184             (sinh(2*pi * t1))) * (tanh((pi - theta) * t1))) ...
185             + (((1 + cosh(2*theta*t2)) / (sinh(2*pi*t2))) * ...
186             (tanh((pi - theta) * t2))));
187     end
188 
189     M(tq) = (-pi * R * D * (c_s - c_inf) * (sin(theta) / ...
190         (1 + cos(theta)) + 4 * sum(M_int))) * ...
191         (10^6)*time_step; %converting to ug, multiply by dt
192 
193 %Rate of Volume loss
194 dV(tq) = Vi + sum(M);
195 end
196 
197 %% Plots
198     %Generalizing data to plot
199     Exp_Vol_plot = Test_Data(:,5)/Vi;
200     Num_Vol_plot = dV/dV(1);
201     if plot_type == 1 %Normalized Volume Plots
202         Exp_time_plot = Test_Data(:,1);
203         Num_time_plot = time;
204         error_time = time;
205         x_label = 'Time, t (s)';
206     elseif plot_type == 2 %Normalized Volume/Time Plots
207         Exp_time_plot = Test_Data(:,1)/max(Test_Data(:,1));
208         Num_time_plot = time/max(time);
209         error_time = time/max(time);
210         x_label = 'Normalized Time (t/\tau_E)';
```

```
211     else
212         disp('Reason for error:')
213         disp('Invalid plot_type Value')
214     end
215 
216     figure(1)
217         set(gca,'FontSize',20)
218         xlabel(x_label)
219         ylabel('Normalized Volume (\forall/\forall_0)')
220         set(gca,'XMinorTick','on')
221         set(gca,'YMinorTick','on')
222         axis([0, 1.1*max(Exp_time_plot), 0, 1.1])
223         axis square
224         box on
225     hold all
226 
227     %Plot styles for numerical data
228     if yn_cs == 1;
229         if yn_pin == 1
230             plot_style = '--';
231         else
232             plot_style = ':';
233         end
234         plot_color = 'black';
235         plot_legend = 'Constant C_s Model';
236         error_marker = 'o';
237         error_legend = '-o';
238         error_edge = 'white';
239             if yn_pin == 1 && yn_cs == 1
240                 plot_legend = 'Pinned Numerical Model';
241             elseif yn_pin == 2
242                 plot_legend = 'Depinned Numerical Model';
243                 error_edge = 'black';
244                 error_facemarker = 'white';
245             end
246     elseif yn_cs == 2;
247         plot_style = '-.';
248         plot_color = 'blue';
249         plot_legend = 'Briones et al. Interpolated C_s';
250         error_marker = 's';
251         error_legend = '-s';
252         error_edge = 'black';
```

```
253     elseif yn_cs == 3;
254         plot_style = '-.';
255         plot_color = 'magenta';
256         plot_legend = 'Dash and Garimella Interpolated C_s';
257         error_marker = 'd';
258         error_legend = '-d';
259         error_edge = 'black';
260     elseif yn_cs == 4;
261         plot_style = ':';
262         plot_color = [0, 0.5, 0];
263         plot_legend = 'Combined C_s Distribution';
264         error_marker = '^';
265         error_legend = '-^';
266         error_edge = 'black';
267     end
268
269
270     p(k*k) = plot(Exp_time_plot,Exp_Vol_plot, ...
271         'Color','red','LineWidth',3);
272     p(k*k+1) = plot(Num_time_plot, Num_Vol_plot, ...
273         'LineStyle', plot_style, 'Color', plot_color, ...
274         'LineWidth',3);
275     if iter == 4
276         if k == 4
277             legend(p([1, 2, 5, 10, 17]),'Experimental Data', ...
278                 'Constant C_s Model', ...
279                 'Briones et al. Interpolated C_s', ...
280                 'Dash and Garimella Interpolated C_s', ...
281                 'Combined C_s Distribution', ...
282                 'Location','NorthEast')
283         end
284     else
285         legend(p([k, k+1]),'Experimental Data', plot_legend, ...
286             'Location','NorthEast')
287     end
288 %% Error Analysis Plots
289 if er == 2;
290     Error = (Test_Data(:,5) - dV') / Vi;
291         fprintf('%s %g %s \n','Max Error =', ...
292             100*max(abs(Error)),'%')
293         fprintf('%s %g %s \n \n','Average Error =', ...
294             100*mean(abs(Error)),'%')
```

```
295
296         figure(2)
297             set(gca,'FontSize',20)
298             xlabel(x_label)
299             ylabel('Error %')
300             set(gca,'XMinorTick','on')
301             set(gca,'YMinorTick','on')
302             box on
303             axis square
304             axis([0, max(error_time), 0, 20])
305         hold all
306
307         for i = 1:length(time)/7-1
308             time_markers(i) = Exp_time_plot(7*i);
309             Error_markers(i) = 100*abs(Error(7*i));
310         end
311
312         %special plot for creating legend
313         pe(k*(k+1)) = plot(-1, -1, error_legend, ...
314                 'LineWidth',2, ...
315                 'Color',plot_color, ...
316                 'Marker',error_marker,'MarkerSize',11, ...
317                 'MarkerFaceColor',plot_color, ...
318                 'MarkerEdgeColor',error_edge);
319             if yn_pin == 2
320                pe(k*(k+1)) = plot(-1, -1, error_legend, ...
321                 'LineWidth',2, ...
322                 'Color',plot_color, ...
323                 'Marker',error_marker,'MarkerSize',11, ...
324                 'MarkerFaceColor',error_facemarker, ...
325                 'MarkerEdgeColor',error_edge);
326             end
327         %Error plot
328         pe(k*(k+1)+1) = plot(Exp_time_plot,100*abs(Error), ...
329             'Linewidth', 2, 'Color', plot_color);
330         pe(k*(k+1)+2) = plot(time_markers,Error_markers, ...
331                 'LineStyle','none', ...
332                 'LineWidth',2, ...
333                 'Marker',error_marker,'MarkerSize',11, ...
334                 'MarkerFaceColor',plot_color, ...
335                 'MarkerEdgeColor',error_edge);
336             if yn_pin == 2;
```

```
337                 pe(k*(k+1)+2) = plot(time_markers,Error_markers, ...
338                     'LineStyle','none', ...
339                     'LineWidth',2, ...
340                     'Marker',error_marker,'MarkerSize',11, ...
341                     'MarkerFaceColor',error_facemarker, ...
342                     'MarkerEdgeColor',error_edge);
343                 end
344
345             if iter == 4
346                 if k == 4
347                     legend(pe([2, 6, 12 , 20]), ...
348                         'Constant C_s Model', ...
349                         'Briones et al. Interpolated C_s', ...
350                         'Dash and Garimella Interpolated C_s', ...
351                         'Combined C_s Distribution', ...
352                         'Location','NorthWest')
353                 end
354             else
355                 legend(pe(k*(k+1)), plot_legend, ...
356                     'Location','NorthEast')
357             end
358     end
359     end
```

REFERENCES

[1] N. Anantharaju, M. Panchagnula, and S. Neti. Evaporating Drops on Patterned Surfaces: Transition from Pinned to Moving Triple Line. *Journal of Colloid and Interface Science*, 337(1):176–182, 2009.

[2] V. Badam, V. Kumar, F. Durst, and K. Danov. Experimental and Theoretical Investigations on Interfacial Temperature Jumps During Evaporation. *Experimental Thermal and Fluid Science*, 32(1):276–292, 2007.

[3] T. Bergman, F. Incropera, A. Lavine, and D. DeWitt. *Fundamentals of Heat and Mass Transfer*. Wiley, 7th edition, 2011.

[4] T. Blake and J. D. Coninck. The Influence of Solid–Liquid Interactions on Dynamic Wetting. *Advances in Colloid and Interface Science*, 96(1–3):21–36, 2002.

[5] E. Bormashenko, A. Musin, and M. Zinigrad. Evaporation of Droplets on Strongly and Weakly Pinning Surfaces and Dynamics of the Triple Line. *Colloids and Surfaces A: Physicochemical and Engineering Aspects*, 385(1–3):235–240, 2011.

[6] C. Bourges-Monnier and M. E. R. Shanahan. Influence of Evaporation on Contact Angle. *Langmuir*, 11(7):2820–2829, 1995.

[7] A. Briones, J. Ervin, L. Byrd, S. Putnam, J. Jones, and A. White. Effect of Accommodation Coefficient, Curvature and Three-Dimensional Flow on the Evaporation Characteristics of Pinned Water Microdroplets. *42nd AIAA Thermophysics Conference*, July 2011.

[8] A. M. Briones, J. S. Ervin, L. W. Byrd, S. A. Putnam, A. White, and J. G. Jones. Evaporation Characteristics of Pinned Water Microdroplets. *Journal of Thermophysics and Heat Transfer*, 26:480–493, 2012.

[9] A. M. Briones, J. S. Ervin, S. A. Putnam, L. W. Byrd, and L. Gschwender. Micrometer-Sized Water Droplet Impingement Dynamics and Evaporation on a Flat Dry Surface. *Langmuir*, 26(16):13272–13286, 2010.

[10] A. M. Briones, J. S. Ervin, S. A. Putnam, L. W. Byrd, and J. G. Jones. A Novel Kinetically-Controlle De-Pinning Model for Evaporating Water Microdroplets. *International Communications in Heat and Mass Transfer*, 39(9):1311–1319, 2012.

[11] A. B. D. Cassie and S. Baxter. Wettability of Porous Surfaces. *Transactions of the Faraday Society*, 40:546, 1944.

[12] Y. Cengel and M. Boles. *Thermodynamics: An Engineering Approach*. McGraw-Hill Education, 2010.

[13] S. Chandra, M. di Marzo, Y. Qiao, and P. Tartarini. Effect of Liquid-Solid Contact Angle on Droplet Evaporation. *Fire Safety Journal*, 27(2):141–158, 1996.

[14] B. Chichkov, C. Momma, S. Nolte, F. Alvensleben, and A. Tünnermann. Femtosecond, Picosecond and Nanosecond Laser Ablation of Solids. *Applied Physics A*, 63(2):109–115, 1996.

[15] E. F. Crafton and W. Black. Heat Transfer and Evaporation Rates of Small Liquid Droplets on Heated Horizontal Surfaces. *International Journal of Heat and Mass Transfer*, 47(6–7):1187–1200, 2004.

[16] S. Dash and S. V. Garimella. Droplet Evaporation Dynamics on a Superhydrophobic Surface with Negligible Hysteresis. *Langmuir*, 29(34):10785–10795, 2013.

[17] S. David, K. Sefiane, and L. Tadrist. Experimental Investigation of the Effect of Thermal Properties of the Substrate in the Wetting and Evaporation of Sessile Drops. *Colloids and Surfaces A: Physicochemical and Engineering Aspects*, 298(1–2):108–114, 2007.

[18] P. G. de Gennes. Wetting: Statics and Dynamics. *Rev. Mod. Phys.*, 57:827–863, Jul 1985.

[19] R. D. Deegan, O. Bakajin, T. F. Dupont, G. Huber, S. R. Nagel, and T. A. Witten. Capillary Flow as the Cause of Ring Stains from Dried Liquid Drops. *Nature*, 389(6653):827–829, 1997.

[20] R. D. Deegan, O. Bakajin, T. F. Dupont, G. Huber, S. R. Nagel, and T. A. Witten. Contact Line Deposits in an Evaporating Drop. *Phys. Rev. E*, 62:756–765, Jul 2000.

[21] W. Deng and A. Gomez. Electrospray Cooling for Microelectronics. *International Journal of Heat and Mass Transfer*, 54(11–12):2270–2275, 2011.

[22] V. Dugas, J. Broutin, and E. Souteyrand. Droplet Evaporation Study Applied to DNA Chip Manufacturing. *Langmuir*, 21(20):9130–9136, Sept. 2005.

[23] H. Eral, D. 't Mannetje, and J. Oh. Contact Angle Hysteresis: A Review of Fundamentals and Applications. *Colloid and Polymer Science*, 291(2):247–260, 2013.

[24] H. Y. Erbil. Evaporation of Pure Liquid Sessile and Spherical Suspended Drops: A Review. *Advances in Colloid and Interface Science*, 170(1–2):67–86, 2012.

[25] H. Y. Erbil and C. E. Cansoy. Range of Applicability of the Wenzel and Cassie-Baxter Equations for Superhydrophobic Surfaces. *Langmuir*, 25(24):14135–14145, 2009. PMID: 19630435.

[26] C. Extrand. Water Contact Angles and Hysteresis of Polyamide Surfaces. *Journal of Colloid and Interface Science*, 248(1):136–142, 2002.

[27] G. Fang and C. Ward. Temperature Measured Close to the Interface of an Evaporating Liquid. *Physical Review E*, 59:417–428, Jan. 1999.

[28] L. Gao and T. J. McCarthy. How Wenzel and Cassie Were Wrong. *Langmuir*, 23(7):3762–3765, 2007.

[29] H. Gelderblom, A. G. Marín, H. Nair, A. van Houselt, L. Lefferts, J. H. Snoeijer, and D. Lohse. How Water Droplets Evaporate on a Superhydrophobic Substrate. *Phys. Rev. E*, 83:026306, Feb 2011.

[30] F. Girard, M. Antoni, S. Faure, and A. Steinchen. Influence of Heating Temperature and Relative Humidity in the Evaporation of Pinned Droplets. *Colloids and Surfaces A: Physicochemical and Engineering Aspects*, 323(1–3):36–49, 2008.

[31] F. Girard, M. Antoni, and K. Sefiane. On the Effect of Marangoni Flow on Evaporation Rates of Heated Water Drops. *Langmuir*, 24(17):9207–9210, 2008. PMID: 18671417.

[32] R. J. Good. A Thermodynamic Derivation of Wenzel's Modification of Young's Equation for Contact Angles; Together with a Theory of Hysteresis. *Journal of the American Chemical Society*, 74(20):5041–5042, 1952.

[33] H. Hu and R. G. Larson. Evaporation of a Sessile Droplet on a Substrate. *The Journal of Physical Chemistry B*, 106(6):1334–1344, 2002.

[34] H. Hu and R. G. Larson. Analysis of the Effects of Marangoni Stresses on the Microflow in an Evaporating Sessile Droplet. *Langmuir*, 21(9):3972–3980, 2005.

[35] H. Hu and R. G. Larson. Analysis of the Microfluid Flow in an Evaporating Sessile Droplet. *Langmuir*, 21(9):3963–3971, 2005.

[36] P. Kelly-Zion, C. Pursell, S. Vaidya, and J. Batra. Evaporation of Sessile Drops Under Combined Diffusion and Natural Convection. *Colloids and Surfaces A: Physicochemical and Engineering Aspects*, 381(1–3):31–36, 2011.

[37] N. Lebedev and R. Silverman. *Special Functions and Their Application*. Selected Russian publications in the mathematical sciences. Englewood Cliffs, 1965.

[38] M. C. Lopes, E. Bonaccurso, T. Gambaryan-Roisman, and P. Stephan. Influence of the Substrate Thermal Properties on Sessile Droplet Evaporation: Effect of Transient Heat Transport. *Colloids and Surfaces A: Physicochemical and Engineering Aspects*, 432(0):64–70, 2013.

[39] A. Marmur. Contact Angle Hysteresis on Heterogeneous Smooth Surfaces. *Journal of Colloid and Interface Science*, 168(1):40–46, 1994.

[40] A. Marmur and E. Bittoun. When Wenzel and Cassie Are Right: Reconciling Local and Global Considerations. *Langmuir*, 25(3):1277–1281, 2009.

[41] H. Masoud and J. D. Felske. Analytical Solution for Inviscid Flow Inside an Evaporating Sessile Drop. *Phys. Rev. E*, 79:016301, Jan 2009.

[42] J. Maxwell and W. Niven. *The Scientific Letters Papers of James Clerk Maxwell*, volume 2 of *The Scientific Papers of James Clerk Maxwell*. Cambridge University Press, 1890.

[43] A. J. H. McGaughey and C. A. Ward. Temperature Discontinuity at the Surface of an Evaporating Droplet. *Journal of Applied Physics*, 91(10):6406–6415, 2002.

[44] G. McHale, S. Aqil, N. J. Shirtcliffe, M. I. Newton, and H. Y. Erbil. Analysis of Droplet Evaporation on a Superhydrophobic Surface. *Langmuir*, 21(24):11053–11060, 2005.

[45] G. McHale, S. M. Rowan, M. I. Newton, and M. K. Banerjee. Evaporation and the Wetting of a Low-Energy Solid Surface. *The Journal of Physical Chemistry B*, 102(11):1964–1967, 1997.

[46] R. Mollaret, K. Sefiane, J. R. Christy, and D. Veyret. Experimental and Numerical Investigation of the Evaporation into Air of a Drop on a Heated Surface. *Chemical Engineering Research and Design*, 82(4):471–480, 2004.

[47] F. Mugele and J. Baret. Electrowetting: From Basics to Applications. *Journal of Physics-Condensed Matter*, 17(28):R705–R774, n.d.

[48] T. A. Nguyen, A. V. Nguyen, M. A. Hampton, Z. P. Xu, L. Huang, and V. Rudolph. Theoretical and Experimental Analysis of Droplet Evaporation on Solid Surfaces. *Chemical Engineering Science*, 69(1):522–529, 2012.

[49] T. A. H. Nguyen and A. V. Nguyen. Increased Evaporation Kinetics of Sessile Droplets by Using Nanoparticles. *Langmuir*, 28(49):16725–16728, 2012.

[50] T. A. H. Nguyen and A. V. Nguyen. On the Lifetime of Evaporating Sessile Droplets. *Langmuir*, 28(3):1924–1930, 2012.

[51] M. Nosonovsky. On the Range of Applicability of the Wenzel and Cassie Equations. *Langmuir*, 23(19):9919–9920, 2007.

[52] P. G. Pittoni, C.-C. Chang, T.-S. Yu, and S.-Y. Lin. Evaporation of Water Drops on Polymer Surfaces: Pinning, Depinning and Dynamics of the Triple Line. *Colloids and Surfaces A: Physicochemical and Engineering Aspects*, 432(0):89–98, 2013.

[53] A. Polini, E. Mele, A. G. Sciancalepore, S. Girardo, A. Biasco, A. Camposeo, R. Cingolani, D. A. Weitz, and D. Pisignano. Reduction of Water Evaporation in Polymerase Chain Reaction Microfluidic Devices Based on Oscillating-Flow. *Biomicrofluidics*, 4(3):036502, 2010.

[54] Y. O. Popov. Evaporative Deposition Patterns: Spatial Dimensions of the Deposit. *Phys. Rev. E*, 71:036313, Mar 2005.

[55] P. J. Pritchard. *Fox and McDonald's Introduction to Fluid Mechanics*. John Wiley & Sons, Inc., 8th edition, 2011.

[56] A. Promraksa and L.-J. Chen. Modeling Contact Angle Hysteresis of a Liquid Droplet Sitting on a Cosine Wave-like Pattern Surface. *Journal of Colloid and Interface Science*, 384(1):172–181, 2012.

[57] S. A. Putnam, A. M. Briones, L. W. Byrd, J. S. Ervin, M. S. Hanchak, A. White, and J. G. Jones. Microdroplet Evaporation on Superheated Surfaces. *International Journal of Heat and Mass Transfer*, 55(21–22):5793–5807, 2012.

[58] S. A. Putnam, A. M. Briones, J. S. Ervin, M. S. Hanchak, L. W. Byrd, and J. G. Jones. Interfacial Heat Transfer During Microdroplet Evaporation on a Laser Heated Surface. *International Journal of Heat and Mass Transfer*, 55(23–24):6307–6320, 2012.

[59] S. Rao. *Applied Numerical Methods for Engineers and Scientists*. Prentice Hall PTR, 2002.

[60] S. M. Rowan, M. I. Newton, and G. McHale. Evaporation of Microdroplets and the Wetting of Solid Surfaces. *The Journal of Physical Chemistry*, 99(35):13268–13271, 1995.

[61] M. A. Saada, S. Chikh, and L. Tadrist. Evaporation of a Sessile Drop with Pinned or Receding Contact Line on a Substrate with Different Thermophysical Properties. *International Journal of Heat and Mass Transfer*, 58(1–2):197–208, 2013.

[62] S. S. Sazhin. Advanced Models of Fuel Droplet Heating and Evaporation. *Progress in Energy and Combustion Science*, 32:162–214, 2006.

[63] F. Schönfeld, K.-H. Graf, S. Hardt, and H.-J. Butt. Evaporation Dynamics of Sessile Liquid Drops in Still Air with Constant Contact Radius. *International Journal of Heat and Mass Transfer*, 51(13–14):3696–3699, 2008.

[64] S. Semenov, V. Starov, R. Rubio, and M. Velarde. Instantaneous Distribution of Fluxes in the Course of Evaporation of Sessile Liquid Droplets: Computer Simulations. *Colloids and Surfaces A: Physicochemical and Engineering Aspects*, 372(1–3):127–134, 2010.

[65] D. H. Shin, S. H. Lee, J.-Y. Jung, and J. Y. Yoo. Evaporating Characteristics of Sessile Droplet on Hydrophobic and Hydrophilic Surfaces. *Microelectron. Eng.*, 86(4-6):1350–1353, Apr. 2009.

[66] B. Sobac and D. Brutin. Thermal Effects of the Substrate on Water Droplet Evaporation. *Phys. Rev. E*, 86:021602, Aug 2012.

[67] H. Song, Y. Lee, S. Jin, H.-Y. Kim, and J. Y. Yoo. Prediction of Sessile Drop Evaporation Considering Surface Wettability. *Microelectron. Eng.*, 88(11):3249–3255, Nov. 2011.

[68] A. F. Stalder, T. Melchior, M. Müller, D. Sage, T. Blu, and M. Unser. Low-Bond Axisymmetric Drop Shape Analysis for Surface Tension and Contact Angle Measurements of Sessile Drops. *Colloids and Surfaces A: Physicochemical and Engineering Aspects*, 364(1–3):72–81, 2010.

[69] V. Starov and K. Sefiane. On Evaporation Rate and Interfacial Temperature of Volatile Sessile Drops. *Colloids and Surfaces A: Physicochemical and Engineering Aspects*, 333(1–3):170–174, 2009.

[70] R. Tadmor and P. S. Yadav. As-Placed Contact Angles for Sessile Drops. *Journal of Colloid and Interface Science*, 317(1):241–246, 2008.

[71] S. Vedantam and M. V. Panchagnula. Phase Field Modeling of Hysteresis in Sessile Drops. *Phys. Rev. Lett.*, 99:176102, Oct 2007.

[72] D. Von der Linde, K. Sokolowski-Tinten, and J. Bialkowski. Laser–Solid Interaction in the Femtosecond Time Regime. *Applied Surface Science*, 109:1–10, 1997.

[73] R. N. Wenzel. Resistance of Solid Suraces to Wetting by Water. *Industrial & Engineering Chemistry*, 28(8):988–994, 1936.

[74] T. Young. An Essay on the Cohesion of Fluids. *Philosophical Transactions of the Royal Society of London*, 95:65–87, 1805.

[75] Y.-S. Yu, Z. Wang, and Y.-P. Zhao. Experimental and Theoretical Investigations of Evaporation of Sessile Water Droplet on Hydrophobic Surfaces. *Journal of Colloid and Interface Science*, 365(1):254–259, 2012.

[76] J. X. Zhou, J. Y. H. Fuh, L. Han Tong, W. Yoke San, N. Yuan Song, J. J. Gray, and C. Soo Jin. Characterization of Drop-on-Demand Microdroplet Printing. *International Journal of Advanced Manufacturing Technology*, 48(1-4):243–250, 2010.

[77] Z.-Q. Zhu and Q.-S. Liu. Interfacial Temperature Discontinuities in a Thin Liquid Layer During Evaporation. *Microgravity Science and Technology*, 25(4):243–249, 2013.